5. THE ARCTIC—J. Richter-Menge and J. Mathis, Eds.

a. Introduction—J. Richter-Menge and J. Mathis

The Arctic chapter describes a range of observations of essential climate variables (ECV; Bojinski et al. 2014) and other physical environmental parameters, encompassing the atmosphere, ocean, and land in the Arctic and subarctic. As in previous years, the 2015 report illustrates that although there are regional and seasonal variations in the state of the Arctic environmental system, it continues to respond to long-term upward trends in air temperature. Over Arctic landmasses, the rate of warming is more than twice that of low and midlatitude regions.

In 2015, the average annual surface air temperature anomaly over land north of 60°N was +1.2°C, relative to the 1981–2010 base period. This ties the recent years of 2007 and 2011 for the highest value in the temperature record starting in 1900 and represents a 2.8°C increase since the beginning of the 20th century. Evidence of strong connections between the Arctic and midlatitude regions occurred from 1) November 2014 through June 2015, when anomalously warm conditions in the Pacific Arctic region were associated with southerly air flow into and across Alaska, and 2) February through April 2015, when anomalously cold conditions from northeastern North America to southwest Greenland were associated with northerly air flow.

There is clear evidence of linkages among the various components of the Arctic system. Under the influence of persistent warming temperatures, the Arctic sea ice cover is diminishing in extent and thickness. The lowest maximum sea ice extent in the 37-year satellite record occurred on 25 February 2015, at 7% below the average for 1981–2010. This date of occurrence was the second earliest in the record and 15 days earlier than the average date of 12 March. Minimum sea ice extent in September 2015 was 29% less than the 1981–2010 average and the fourth lowest value in the satellite record. In February and March, the oldest ice (>4 years) and first-year ice made up 3% and 70%, respectively, of the pack ice compared to values of 20% and 35%, respectively, in 1985.

As the extent of sea ice retreat in the summer continues to increase, allowing previously ice-covered water to be exposed to more solar radiation, sea surface temperature (SST) and upper ocean temperatures are increasing throughout much of the Arctic Ocean and adjacent seas. The Chukchi Sea northwest of Alaska and eastern Baffin Bay off west Greenland have the largest warming trends: ~0.5°C per decade since 1982. In 2015, SST was up to 4°C higher than the 1982–2010 average in eastern Baffin Bay and the Kara Sea north of central Eurasia.

The impact of sea ice retreat and warming ocean temperatures on the ecosystem is well demonstrated by changes in the behavior of walrus and fish communities. In the Pacific Arctic, vast walrus herds are now hauling out on land rather than on sea ice as the ice retreats far to the north over the deep Arctic Ocean, raising concern about the energetics of females and young animals. Warming trends in water temperatures in the Barents Sea, which started in the late 1990s, are linked to a community-wide shift in fish populations: boreal communities are now found farther north and the local Arctic (cold-water affinity) community has been almost pushed out of the area.

Ice on land, including glaciers and ice caps outside Greenland (Arctic Canada, Alaska, Northern Scandinavia, Svalbard, and Iceland) and the Greenland Ice Sheet itself, continues to lose mass. In 2015, the Greenland Ice Sheet, with the capacity to contribute ~7 m to sea level rise, experienced melting over more than 50% of the ice sheet for the first time since the exceptional melting of 2012 and exceeded the 1981–2010 average on 50 of 92 days (54%). Reflecting the pattern of ice melt, which is driven by the pattern of surface air temperature anomalies, the average albedo in 2015 was below the 2000–09 average in northwest Greenland and above average in southwest Greenland.

Despite above-average snow cover extent (SCE) in April, Arctic SCE anomalies in May and June 2015 were below the 1981–2010 average, a continuation of consistent early spring snowmelt during the past decade. June SCE in both the North American and Eurasian sectors of the Arctic was the second lowest in the satellite record (1967–present). The rate of June SCE reductions since 1979 (the start of the passive microwave satellite era) is 18% per decade.

In 2014, the most recent year with complete data, the combined discharge of the eight largest Arctic rivers [2487 km^3 from Eurasia (Pechora, S. Dvina, Ob', Yenisey, Lena, and Kolyma) and North America (Yukon and Mackenzie)] was 10% greater than the average discharge during 1980–89. Since 1976, discharge of the Eurasian and North American rivers has increased 3.1% and 2.6% per decade, respectively.

Regional variability in permafrost temperature records indicates more substantial permafrost warming since 2000 in higher latitudes than in the subarctic, in agreement with the pattern of average air temperature anomalies. In 2015, record high temperatures at 20-m depth were measured at all permafrost observatories on the North Slope of Alaska, increasing between

0.21°C and 0.66°C decade^{-1} since 2000. Permafrost warming in northernmost Alaska exemplifies what is happening to permafrost on a pan-Arctic scale.

Arctic cloud cover variability significantly influences ultraviolet index (UVI) anomaly patterns. Reflecting this influence, monthly average noontime UVIs for March 2015 were below the 2005–14 means in a belt stretching from the Greenland Sea and Iceland in the east to Hudson Bay and the Canadian Arctic Archipelago in the west. This region roughly agrees with the regions where the atmospheric total ozone columns (TOC) were abnormally high in March 2015. At the pan-Arctic scale, the minimum TOC in March was 389 Dobson Units (DU), 17 DU (5%) above the average of 372 DU for the period 1979–2014 and 23 DU (6%) above the average for the past decade (2000–14).

This overview alone refers to a number of different periods of observation for which average values and departures from average (anomalies) have been calculated. For the World Meteorological Organization, and national agencies such as NOAA, 1981–2010 is the current standard reference period for calculating climate normals (averages) and anomalies. In this report, the current standard reference period is used when possible, but it cannot be used for all the variables described; some organizations choose not to use 1981–2010 and many observational records postdate 1981. The use of different periods to describe the state of different elements of the Arctic environmental system is unavoidable, but it does not change the fact that change is occurring throughout the Arctic environmental system.

b. Air temperature—J. Overland, E. Hanna, I. Hanssen-Bauer, S.-J. Kim, J. Walsh, M. Wang, U. S. Bhatt, and R. L. Thoman

Arctic air temperatures are both an indicator and a driver of regional and global changes. Although there are year-to-year and regional differences in air temperatures due to natural variability, the magnitude and Arctic-wide character of the long-term temperature increase are major indicators of global warming (Overland 2009).

The mean annual surface air temperature anomaly for 2015 for land stations north of 60°N was +1.2°C, relative to the 1981–2010 mean value (Fig. 5.1). This ties the recent years of 2007 and 2011 for the highest value in the record starting in 1900. Currently, the Arctic is warming at more than twice the rate of lower latitudes (Fig. 5.1).

The greater rate of Arctic temperature increase compared to the global increase is referred to as Arctic amplification. Mechanisms for Arctic amplification include reduced summer albedo due to sea ice and snow cover loss, the decrease of total cloudiness in summer and an increase in winter, and the additional heat generated by increased sea ice free ocean areas that are maintained later into the autumn (Serreze and Barry 2011; Makshtas et al. 2011). Arctic amplification is also enhanced because radiational loss of heat from the top of the atmosphere is less in the Arctic than in the subtropics (Pithan and Mauritsen 2014).

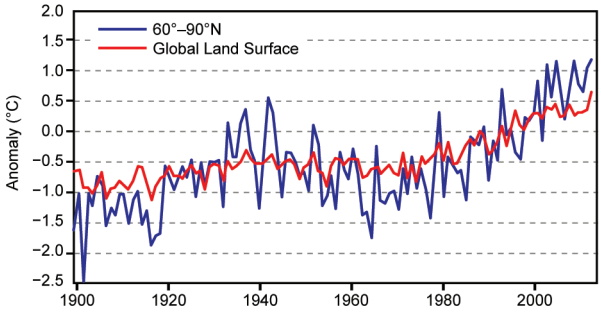

Fig. 5.1. Arctic (land stations north of 60°N) and global mean annual land surface air temperature (SAT) anomalies (in °C) for the period 1900–2015 relative to the 1981–2010 mean value. Note that there were few stations in the Arctic, particularly in northern Canada, before 1940. (Source: CRUTEM4.)

Although there is an Arctic-wide long-term pattern of temperature increases, regional differences can be manifest in any given season based on natural variability of the atmospheric circulation (Overland et al. 2011; Kug et al. 2015).

Seasonal air temperature anomalies are described in Fig. 5.2 for winter [January–March (JFM)], spring [April–June (AMJ)], summer [July–September (JAS)], and autumn [October–December (OND)] of 2015. All seasons show extensive positive temperature anomalies across the central Arctic with many regional seasonal temperature anomalies greater than +3°C, relative to a 1981–2010 base period.

Warm temperature anomalies in winter 2015 extended across the Arctic, from the Pacific sector to the Atlantic sector (Fig. 5.2a). The warmest temperature anomalies were centered on Alaska and far eastern Siberia, including the Chukchi and East Siberian Seas. In Svalbard, in the Atlantic sector northeast of Greenland, winter temperatures were typically 2°C above the 1981–2010 average. In contrast, cold (negative) temperature anomalies of –2° to –3°C extended from southwest Greenland to central Canada and into the eastern United States.

A broad swath of warm temperature anomalies continued to stretch across the Arctic in spring

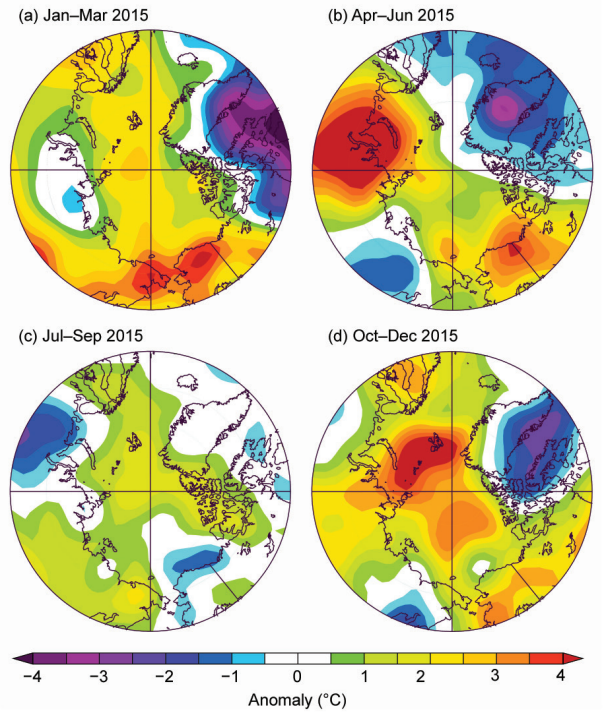

Fig. 5.2. 2015 Seasonal anomaly patterns for near-surface air temperatures (°C) relative to the baseline period 1981–2010 in (a) winter, (b) spring, (c) summer, and (d) autumn. Temperatures are from somewhat above the surface layer (at 925 mb level) to emphasize large spatial patterns rather than local features. (Source: NOAA/ESRL.)

2015, with a continuing warm anomaly over Alaska (Fig. 5.2b). However, unlike the winter pattern (Fig. 5.2a), spring saw a shift to a very warm anomaly (+4°C) over central Eurasia. A significant cold anomaly (–3°C) was centered over Greenland. In contrast to Greenland, spring temperatures at the weather station in Svalbard were typically 2°C above the 1981–2010 average, as Svalbard was located on the margin of the broad swath of positive temperature anomalies that extended from Alaska to Eurasia.

A warm temperature anomaly over much of the Arctic Ocean, with the exception of a moderately cold anomaly over the Beaufort Sea north of Alaska, characterized summer 2015 (Fig. 5.2c). Particularly cold anomalies occurred over western Eurasia. As noted in section 5f, a new record August low temperature of –39.6°C occurred on 28 August at Summit (elevation 3216 m in the center of the ice sheet), while summer temperatures measured at most coastal weather stations were above average (Tedesco et al. 2015). Similar to coastal Greenland locations, at the Svalbard weather station the average temperature was 1°–2°C above the 1981–2010 average, the highest JAS average ever recorded in the composite Longyearbyen–Svalbard Airport record that dates to 1898 (Nordli et al. 2014).

In autumn, particularly warm air temperature anomalies were seen in the subarctic regions of the Barents and Bering Seas (Fig. 5.2d). While the central Arctic remained relatively warm, cold anomalies were seen in northeastern North America similar to winter 2015. A difference, however, is that central Asia was also relatively cold in autumn compared to the warmer previous winter.

Both winter and autumn 2015 illustrate extensive interaction of large-scale weather systems between the Arctic and midlatitudes. The anomalously warm temperatures across Alaska in winter and spring 2015 (Fig. 5.2a,b) extend a pattern that began during autumn 2014. The persistent positive (warm) near-surface air temperature anomalies in Alaska and extending into the Chukchi and Beaufort Seas were associated with warm sea surface temperatures in the Gulf of Alaska and a pattern of geopotential height anomalies characterized by higher values along the Pacific Northwest coast of North America and lower values farther offshore (Fig. 5.3a). Consequently, warm air over the northeast Pacific Ocean was advected by southerly winds into and across Alaska, contributing to high mass loss on glaciers (see section 5f). Associated with the southerly winds, a downslope component of the wind on the north side of the Alaska Range and into Interior Alaska caused dry conditions and reinforced high temperatures. The warm and dry conditions in Interior Alaska during May and June contributed to the second worst fire season on record for those months, eclipsed only by 2004.

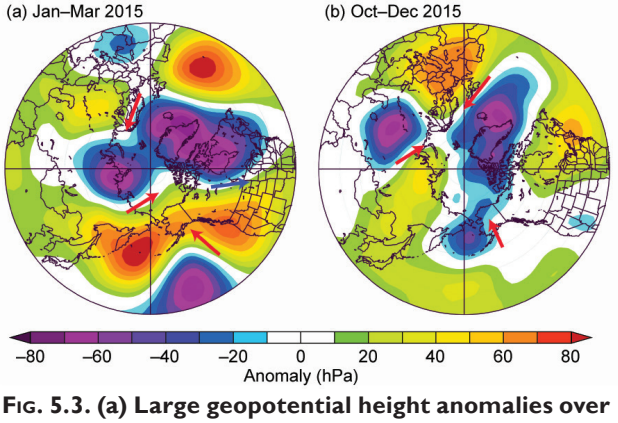

Fig. 5.3. (a) Large geopotential height anomalies over western and eastern North America and continuing into the North Atlantic sector in winter 2015. (b) Negative geopotential height anomalies over the North Atlantic and Bering Sea sectors in autumn 2015. The arrows indicate anomalous warm (red) and cold (blue) air flow generated as a result of these anomaly patterns.

In contrast to the warm temperature anomalies in winter in Alaska (Fig. 5.2a) due to warm, southerly air flow (Fig. 5.3a), the cold anomalies extending from eastern Canada to southwest Greenland (Fig. 5.2a) were associated with strong northwesterly air flow. These cold anomalies extended into early spring. The potential source of these relatively cold temperatures is illustrated by the extensive winter (JFM) negative geopotential height anomaly pattern (Fig. 5.3a) that shows high values over northwestern North America and low values over eastern North America, Greenland, and across the central Arctic Ocean to central Eurasia. Northwesterly winds on the west side of the trough between the two height centers channeled cold air southward from the source region in the central Arctic into northeastern North America. This geopotential height anomaly pattern may also explain the above-average winter air temperatures in Svalbard, which were associated with warm air advection across western Eurasia and into the central Arctic Ocean (Figs. 5.2a,b).

Autumn 2015 was noted for large active low pressure systems in the North Atlantic and Bering Sea (Fig 5.3b). These low height anomaly patterns with southerly wind components to their east kept the Chukchi and Barents Seas relatively warm and sea ice free well into the autumn season.

c. Sea ice cover—D. Perovich, W. Meier, M. Tschudi, S. Farrell, S. Gerland, and S. Hendricks

Three key variables are used to describe the state of the ice cover: the ice extent, the age of the ice, and the ice thickness. Sea ice extent is used as the basic description of the state of Arctic sea ice cover. Satellite-based passive microwave instruments have been used to determine sea ice extent since 1979. There are two months each year that are of particular interest: September, at the end of summer, when the ice reaches its annual minimum extent, and March, at the end of winter, when the ice typically reaches its maximum extent. Maps of monthly average ice extents in March 2015 and September 2015 are shown in Fig. 5.4.

Based on estimates produced by the National Snow and Ice Data Center (NSIDC), the 2015 sea ice cover reached its maximum extent on 25 February, at a value of 14.54 million km^2. This was 7% below the 1981–2010 average and the lowest maximum value in the satellite record. Also notable, the maximum extent occurred 15 days earlier than the 1981–2010 average (12 March) and was the second earliest of the satellite record. The annual minimum extent of 4.41 million km^2 was reached on 11 September. This was substantially higher (30%) than the record minimum of 3.39 million km^2 set in 2012. However, the 2015 summer minimum extent was still 1.81 million km^2 (29%) less than the 1981–2010 average minimum ice extent and 0.62 million km^2 (12%) less than the 2014 minimum.

Sea ice extent has decreasing trends in all months and nearly all regions (the exception being the Bering Sea during winter). In 2015, the largest losses were in the eastern Arctic in regions of warm air temperature anomalies in spring and summer (section 5b, Fig. 5.2). The September monthly average decline for the entire Arctic Ocean is now –13.4% decade^{-1} relative to the 1981–2010 average (Fig. 5.5). The trend is smaller dur-

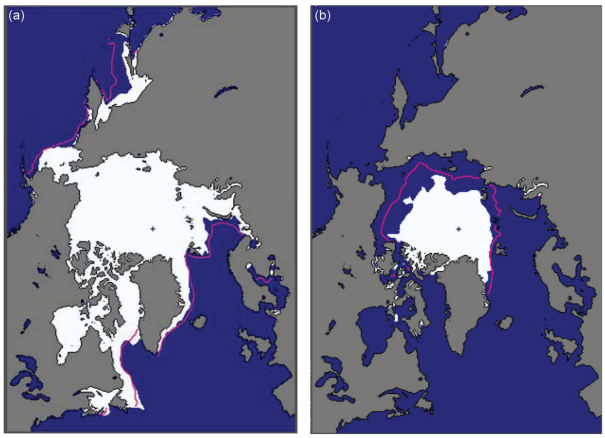

Fig. 5.4. Average sea ice extent in (a) Mar and (b) Sep 2015 illustrate the respective winter maximum and summer minimum extents. The magenta line indicates the median ice extents in Mar and Sep, respectively, during the period 1981–2010. (Source: NSIDC.)

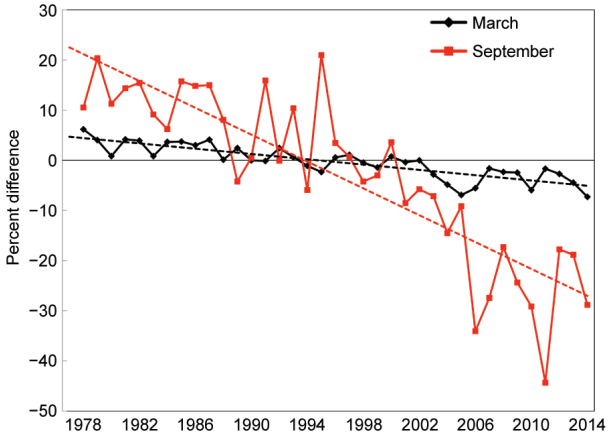

Fig. 5.5. Time series of ice extent anomalies in Mar (the month of maximum ice extent) and Sep (the month of minimum ice extent). The anomaly value for each year is the difference (in %) in ice extent relative to the mean values for the period 1981–2010. The black and red lines are least squares linear regression lines. Both trends are significant at the 99% confidence level.

ing March (–2.6% decade^{-1}) but is still a statistically significant rate of decrease in sea ice extent.

Prior to 2007, there had not been a March to September loss of more than 10 million km^2 of ice in the record, but now such large losses are not unusual. More typical of recent years, 10.13 million km^2 of ice was lost between the March maximum and September minimum extent in 2015.

The age of sea ice serves as an indicator for ice physical properties, including surface roughness, melt pond coverage, and thickness. Older ice tends to be thicker and thus more resilient to changes in atmospheric and oceanic forcing than younger ice. The age of the ice is estimated using satellite observations and drifting buoy records to track ice parcels over several years (Tschudi et al. 2010; Maslanik et al. 2011). This method has been used to provide a record of the age of the ice since the early 1980s (Tschudi et al. 2015).

The oldest ice (>4 years old) continues to make up a small fraction of the Arctic ice pack in March, when the sea ice extent has been at its maximum in most years of the satellite record (Figs. 5.6a,b). In 1985, 20% of the ice pack was >4 years old, but in March 2015, this ice category only constituted 3% of the ice pack. Furthermore, we note that first-year ice now dominates the ice cover, comprising ~70% of the March 2015 ice pack, compared to about 50% in the 1980s. Given that older ice tends to be thicker, the sea ice cover has transformed from a strong, thick pack in the 1980s to a more fragile, thin, and younger pack in recent years. The thinner, younger ice is more vulnerable to melting out in the summer, resulting in lower minimum ice extents. The distribution of ice age in March 2015 was similar to that in March 2014 (Fig. 5.6a).

Most of the oldest ice accumulates along the coast of North Greenland and the Queen Elizabeth Islands of the Canadian Arctic Archipelago, and much of this ice has resided in this area for several years (Fig. 5.6b). In 2015, as in most years, ice transport patterns resulted in the movement of old ice from this area into the Beaufort Sea. The lack of ice older than one year in the eastern Arctic (on the Eurasian side of the Arctic basin) foreshadows its susceptibility to melt out in summer. The ice in the southern Beaufort and Chukchi Seas has also melted completely in the past few summers, with even the oldest ice not surviving the season.

Observations of sea ice thickness and volume from multiple sources have revealed the continued decline of the Arctic sea ice pack over the last decade (Kwok and Rothrock 2009; Laxon et al. 2013; Kwok and Cunningham 2015). Figure 5.6c shows ice thicknesses derived from CryoSat-2 satellite results and IceBridge aircraft observations in March–April 2015. The oldest ice north of Greenland and the Canadian Arctic Archipelago remains thicker than 3 m. There is a strong gradient to thinner, seasonal ice in the Canada basin and the eastern Arctic Ocean, where ice is 1–2 m thick.

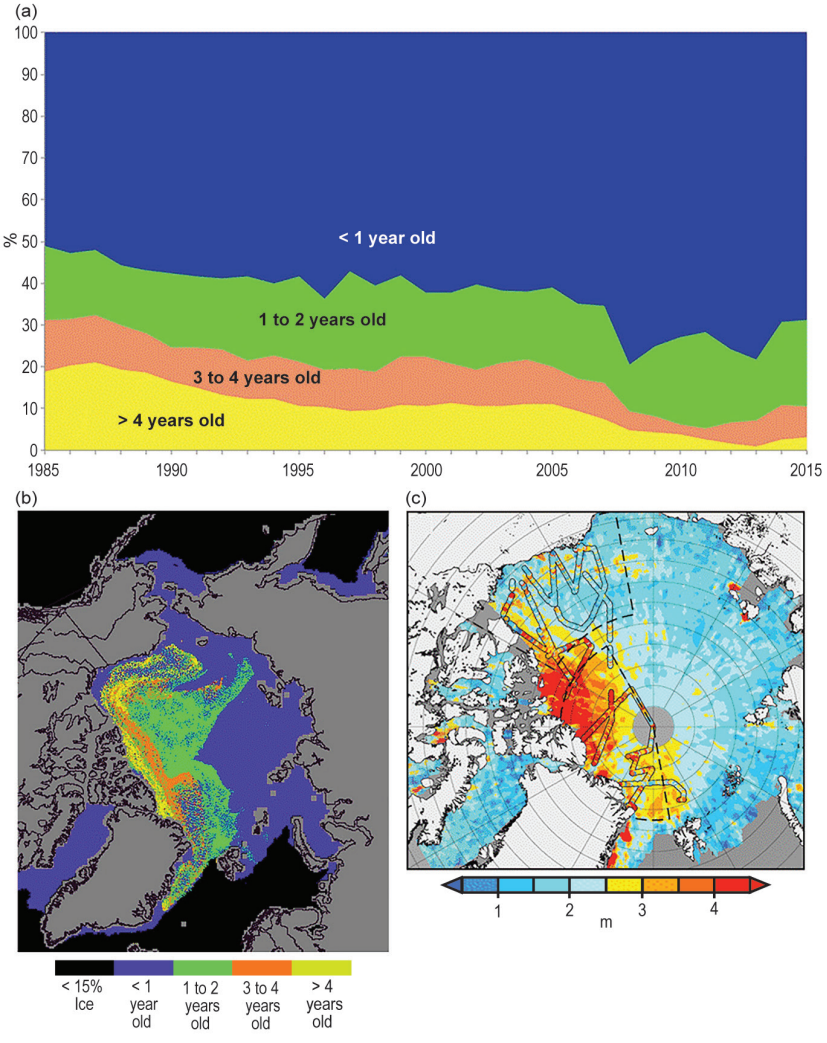

Fig. 5.6. (a) Time series of sea ice age in Mar for 1985–present, (b) sea ice age in Mar 2015, and (c) sea ice thickness derived from ESA CryoSat-2 (background map) and NASA Operation IceBridge measurements (color coded lines) for Mar/Apr 2015.

SIDEBAR 5.1: WALRUSES IN A TIME OF CLIMATE CHANGE—

K. M. KOVACS, P. LEMONS, AND C. LYDERSEN

Climate change-induced alterations in Arctic ecosystems are having impacts at all trophic levels, which are already being described as "transformative" (Johannessen and Miles 2011). However, it remains a challenge to predict impacts in terms of population trends of even highly visible, top trophic animals on multidecadal scales, based on changes occurring in primary physical features that determine habitat suitability. For example, sea ice declines are clearly a major threat to ice-associated marine mammals (e.g., Kovacs et al. 2012; Laidre et al. 2015), but documented regional patterns in sea ice losses are not necessarily reflected in the trajectories of ice-dependent marine mammal populations on a regional basis. In this regard, walruses (*Odobenus rosmarus*) make an interesting case study.

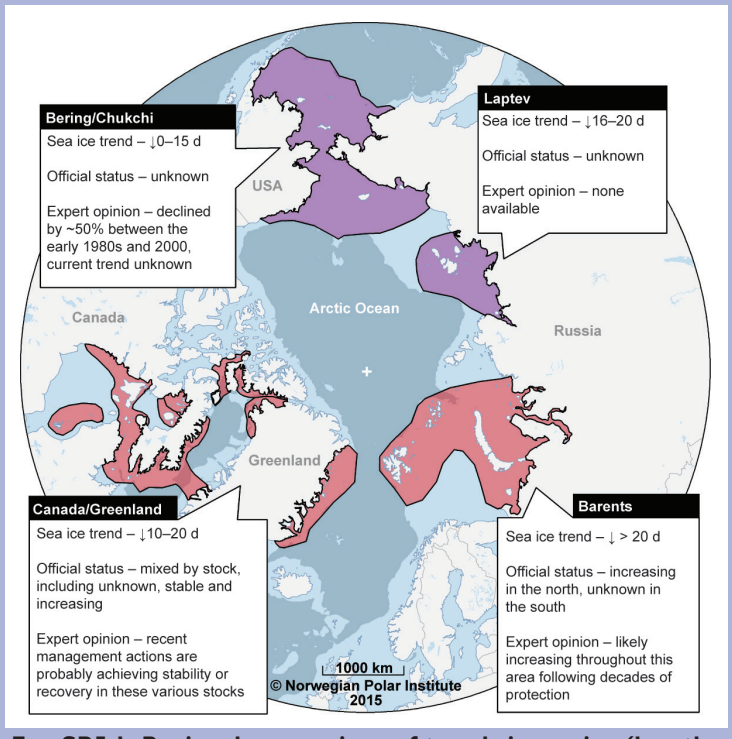

FIG. SB5.1. Regional comparison of trends in sea ice (length of the summer season – number of days less coverage decade^{-1}) and walrus stocks according to Laidre et al. (2015) and expert opinion for Pacific (purple) and Atlantic walrus (red) by region. Stocks are identified by black boundary lines.

Walruses of both subspecies, *O. r. divergens* in the North Pacific Arctic and *O. r. rosmarus* in the North Atlantic Arctic, mate along ice edges in the drifting pack ice during winter and give birth on sea ice in the late spring. Both subspecies use sea ice extensively as a haul-out platform throughout much of the year if it is available close enough to foraging areas. This habitat also provides shelter from storms and protection from some predators. Despite these shared critical links to sea ice, the population trajectories for the two subspecies do not consistently reflect the relative patterns of sea ice losses in the two broad regions occupied by the two subspecies.

The latest research indicates that the Pacific walrus population in the Bering and Chukchi Seas likely declined from about 1980 to 2000 (Taylor and Udevitz 2015). Prior to this time, subsistence harvest restrictions had allowed this population to recover from earlier overexploitation (Fay et al. 1989) to a level that likely approached the carrying capacity of the environment (e.g., Hills and Gilbert 1994). But, population models suggest that a subsequent decline of approximately 50% took place in the Pacific population (Taylor and Udevitz 2015), which was likely initially stimulated by changes in vital rates (e.g., birth rates, calf survivorship) within the population. This decline has almost certainly been exacerbated by declines in sea ice in the region (Fig. SB5.1), associated with global climate change (Taylor and Udevitz 2015). Hypothesized mechanisms include: (1) the retreat of sea ice to a position over the deep Arctic Ocean basin, forcing walruses to use land-based haulouts where trampling increases mortality of young animals (Fischbach et al. 2009; Udevitz et al. 2012) and (2) the decline in sea ice reducing walruses' access to prey, which could impact the adult female body condition, ultimately reducing calf survival and recruitment (Jay et al. 2011; Taylor and Udevitz 2015). The use of land-based haulout areas is not novel for Pacific walruses, but females with dependent young typically utilize sea ice for hauling out (Fay 1982), which allows them to avoid particularly large land-based groups where crowding and trampling events can result in high calf mortality. A lack of sea ice over the shelf in summer in the Bering and Chukchi Seas is already resulting in increased use of coastlines and islands by females with calves, which has in turn resulted in significant calf mortalities in recent years (Fishbach et al. 2009). Additionally, there is ongoing concern about the impacts of declining sea ice on the future energetics of females and young animals. These conditions require the animals to take significantly longer feeding trips between the coastal haul outs and offshore areas with high prey abundance (180 km one-way), rather than utilizing nearby ice edges for resting as they did in the past.

Sea ice losses in the North Atlantic Arctic, in particular the Barents Sea region, have been much more extreme than in the North Pacific (Fig. SB5.1). But, Atlantic walrus abundance is increasing or stable for all stocks for which the trend is known (see Laidre et al. 2015) despite reductions in carrying capacity that are almost certainly taking place due to the sea ice declines. Concern does remain regarding possible overharvesting of several stocks with currently unknown trends in Canada/Greenland. However, the positive turnarounds that have occurred are responses to protective management regimes that have been instituted in the early- and mid-1900s (1928 in Canada, 1952 in Norway, and 1956 in Russia), and, in the case of Greenland, much more recently, with quotas being established there in 2006 (see Wiig et al. 2014 for more details). Perhaps the most extreme example of walrus abundance increasing where environmental conditions are deteriorating due to climate change occurs in the Svalbard Archipelago. Svalbard is an Arctic hot spot that is experiencing dramatic sea ice declines and warming ocean and air temperatures, and yet walrus numbers in the archipelago are increasing exponentially (Kovacs et al. 2014). Walruses in this area were hunted without restriction over several hundred years, up until the 1950s. When they finally became protected in 1952, there were at best a few hundred animals left. Now, after 60 years of complete protection from hunting, with some special no-go reserve areas, recovery is taking place, despite major reductions in sea ice. More females with calves are documented during surveys and historically used sites are being reoccupied as walruses continue to expand through the archipelago. These changes are occurring despite the fact that overall carrying capacity of the region for walruses is likely declining.

The population trajectories of many walrus stocks are currently a result of distant past, or more recent, hunting regimes. However, there is little question that sea ice declines are going to be a challenge for walruses in the future along with other climate change related factors such as increased shipping and development in the north, increased disease and contaminant risks, and ocean acidification impacts on the prey of walruses.

d. Sea surface temperature—M.-L. Timmermans and A. Proshutinsky

Summer sea surface temperatures in the Arctic Ocean are set by absorption of solar radiation into the surface layer. In the Barents and Chukchi Seas, there is an additional contribution from advection of warm water from the North Atlantic and Pacific Oceans, respectively. Solar warming of the ocean surface layer is influenced by the distribution of sea ice (with more solar warming in ice-free regions), cloud cover, water color, and upper-ocean stratification. In turn, warmer SSTs can drive intensified cyclonic activity; cyclones propagating in marginal ice zones are associated with large ocean-to-atmosphere heat fluxes in ice-free regions (e.g., Inoue and Hori 2011). Here, August SSTs are reported, which are an appropriate representation of Arctic Ocean summer SSTs and are not affected by the cooling and subsequent sea ice growth that takes place in the latter half of September. SST data are from the NOAA Optimum Interpolation (OI) SST Version 2 product, which is a blend of in situ and satellite measurements (Reynolds et al. 2002, 2007; www.esrl.noaa.gov/psd/data/gridded/data.noaa.oisst.v2.html).

Mean SSTs in August 2015 in ice-free regions ranged from ~0°C in some places to around +7°C to +8°C in the Chukchi, Barents, and Kara Seas and eastern Baffin Bay off the west coast of Greenland (Fig. 5.7a). August 2015 SSTs show the same general spatial distribution as the August mean for the period 1982–2010 (Timmermans and Proshutinsky 2015; Fig. 5.24b). The August 2015 SST pattern is also similar to that of recent years, for example 2012 (Fig. 5.7b), which was the summer of lowest minimum sea ice extent in the satellite record (1979–present).

Most boundary regions and marginal seas of the Arctic had anomalously warm SSTs in August 2015 compared to the 1982–2010 August mean (Fig. 5.7c). SSTs in these seas, which are mostly ice free in August, are linked to the timing of local sea ice retreat; anomalously warm SSTs (up to +3°C relative to 1982–2010) in August 2015 in the Beaufort and Chukchi Seas were associated with low sea ice extents and exposure of surface waters to direct solar heating (Fig. 5.7c; see also section 5c). The relationship between warm SSTs and reduced sea ice is further apparent in a comparison between August 2015 and August 2014 SSTs: anomalously warm regions (including to the east of Svalbard, where SSTs were up to +3°C warmer in 2015) are associated with relatively lower sea ice extents in 2015 compared to 2014 (Fig. 5.7d). Although SSTs were warmer in general, August 2015 SSTs were cooler relative to average in some regions, for example, along the southern boundaries of the Beaufort and East Siberian Seas (Fig. 5.7c), where summer air temperatures were also below average (see section 5b).

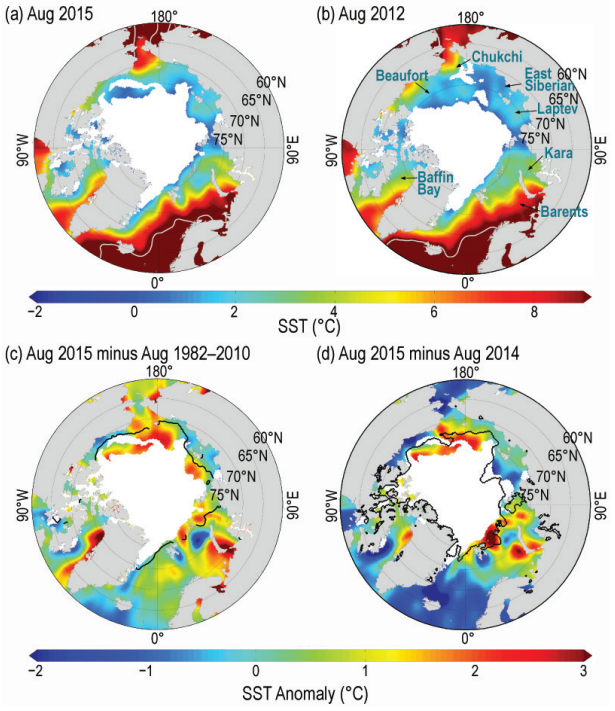

Fig. 5.7. (a) Mean SST (°C) in Aug 2015. White shading is the Aug 2015 mean sea ice extent. (b) Mean SST in Aug 2012. White shading is the Aug 2012 sea ice extent. Gray contours in (a) and (b) indicate the 10°C SST isotherm. (c) SST anomalies (°C) in Aug 2015 relative to the Aug mean for the period 1982–2010. White shading is the Aug 2015 mean ice extent and the black line indicates the median ice edge in Aug for the period 1982–2010. (d) SST anomalies (°C) in Aug 2015 relative to Aug 2014; white shading is the Aug 2015 mean ice extent and the black line indicates the median ice edge for Aug 2014. Sea ice extent and ice edge data are from NSIDC.

Anomalously warm August 2015 SSTs in eastern Baffin Bay were notable, with values as much as 4°C higher than the 1982–2010 August mean; SSTs over the region indicate a general warming trend of about 0.5°C decade^{-1} since 1982 (Fig. 5.8a). Over the past two decades, the linear warming trend in the surface waters of eastern Baffin Bay has accelerated to about 1°C decade^{-1} (+0.10°C yr^{-1}). Along the boundaries of the Arctic basin, the only marginal seas to exhibit statistically significant warming trends are the Chukchi and the Kara Seas. Chukchi Sea August SSTs are warming at a rate of about +0.5°C decade^{-1}, commensurate with declining trends in summer sea ice extent in the region. In the Kara Sea, August 2015 SSTs were also up to 4°C higher than the 1982–2010 August mean; SSTs in this sea have warmed by about +0.3°C decade^{-1} since 1982. In other marginal seas, warm August SST anomalies observed in 2015 are of similar magnitude to warm anomalies observed in past decades (Timmermans and Proshutinsky 2015, their Fig. 5.26a).

The seasonal evolution of SST in the marginal seas exhibited the same general trends and regional differences in 2015 (Fig. 5.8b) as for the preceding decade. Seasonal warming in the marginal seas begins as early as May, and the seasonal cooling period begins as early as mid-August, with cooling observed through December. The asymmetry in rates of seasonal warming and cooling, most notable in the Chukchi Sea and East Baffin Bay, suggests a source of heat in addition to solar radiation. Advection of warm water from the Bering Sea and North Atlantic likely inhibits SST cooling (e.g., Carton et al. 2011; Chepurin and Carton 2012).

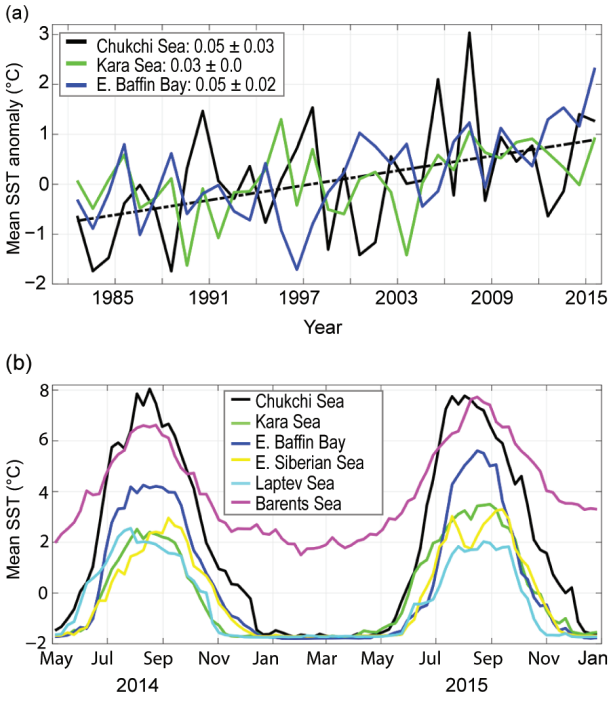

Fig. 5.8. (a) Time series of area-averaged SST anomalies (°C) for Aug of each year relative to the Aug mean for the period 1982–2010 for the Chukchi and Kara Seas and eastern Baffin Bay (see Fig. 5.7b). The dash-dotted black line shows the linear SST trend for the Chukchi Sea (the same warming trend as eastern Baffin Bay). Numbers in the legend correspond to linear trends (with 95% confidence intervals) in °C yr^{-1}. (b) SST (°C) in 2014–15 for each of the marginal seas, where the OISST V2 weekly product has been used in the calculation. For sea ice concentrations greater than 50%, the SST product uses a linear relationship with sea ice concentration to infer SST; variations in freezing temperature as a consequence of salinity variations imply that SSTs inferred from sea ice can be erroneously cool by as much as 0.2°C, with the highest errors in the Canadian sector (see Timmermans and Proshutinsky 2015).

SIDEBAR 5.2: CLIMATE CHANGE IS PUSHING BOREAL FISH NORTHWARD TO THE ARCTIC: THE CASE OF THE BARENTS SEA—M. FOSSHEIM, R. PRIMICERIO, E. JOHANNESEN, R. B. INGVALDSEN, M. M. ASCHAN, AND A. V. DOLGOV

Under climate warming, species tend to shift their distributions poleward (IPCC 2014). Some of the most rapid shifts are taking place in the Arctic, where warming is currently twice the global average (see section 5.b, Fig. 5.1; Hoegh-Guldberg and Bruno 2010; Doney et al. 2012). Poleward shifting marine species have been entering the Arctic Ocean from both the Atlantic and the Pacific (Grebmeier et al. 2010; Wassmann et al. 2011). Boreal (warm-water affinity) species of fish have shifted extensively northward into the Arctic (Mueter and Litzow 2008; Grebmeier et al. 2006; Rand and Logerwell 2011; Christiansen et al. 2013; Fossheim et al. 2015).

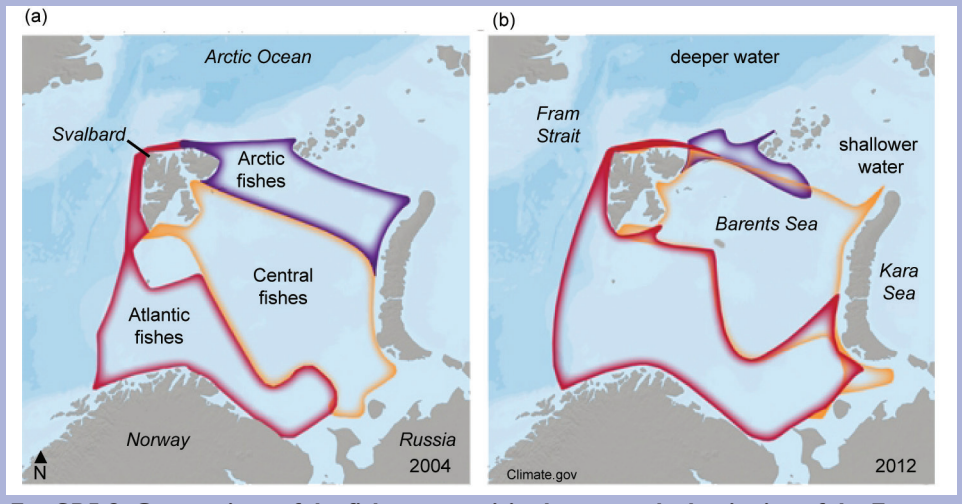

FIG. SB5.2. Comparison of the fish communities between the beginning of the Ecosystem Survey taken in the Barents Sea in (a) 2004 and (b) 2012, indicates a significant change in distribution. The Atlantic (red) and central (yellow) communities (boreal fish species) have shifted north and east, taking over areas previously occupied by the Arctic (blue) community (arctic fish species). Data are available only for the shaded areas. (After Fig. 1 in Fossheim et al. 2015.)

As an example, we present the recent climate-induced changes in the fish communities of the Barents Sea, the entrance point to the Arctic Ocean from the Atlantic. The results are based on a large-scale annual Ecosystem Survey that monitors the whole ice-free shelf of the Barents Sea in August–September, the season with the least sea ice. This cooperative survey between Russia (Knipovich Polar Research Institute of Marine Fisheries and Oceanography) and Norway (Institute of Marine Research) was initiated in 2004. Our focus is on observations for the period 2004–12, as they have been most thoroughly assessed.

In the Barents Sea, the present warming trend in water temperatures started in the late 1990s (Boitsov et al. 2012). The late summer temperature at the seafloor has increased by almost 1°C during the last decade alone. In this region, sub-zero water masses in late summer have almost disappeared and the sea ice is retreating. In association with this warming, boreal fish species have entered the northern parts of the Barents Sea in large numbers. The expansions of these fish species have led to a community-wide shift: boreal communities are now found farther north and the local Arctic (cold-water affinity) community has been almost pushed out of the area (Fig. SB5.2).

The fish species increasing in the north are large boreal fish predators, such as cod (*Gadus morhua*), beaked redfish (*Sebastes mentella*), and long rough dab (*Hippoglossoides platessoides*). These fish species are considered "generalists" in that they can use a wide range of habitats and feed on a diverse set of prey. As such, they are better able to thrive in a changing environment. Their northward expansion is likely related to warmer water temperatures and greater food availability for these fish species (Fossheim et al. 2015). For instance, increased primary productivity in the previously ice-covered area (Dalpadado et al. 2014) and increasing abundance and biomass of Atlantic zooplankton in the northern Barents Sea (Dalpadado et al. 2012) likely favor boreal over Arctic fish species.

Cod, the most important commercial species, has reached a record high population size due to a favorable climate and lower fishing pressure (Kjesbu et al. 2014). The cod stock in the Barents Sea has not been this high since the 1950s. High abundances have also been recorded for haddock (*Melanogrammus aeglefinus*), the other main commercial species, and for long rough dab, a common and widespread species in the Barents Sea. A poleward expansion of cod and haddock and a northeastward displacement of beaked redfish (*Sebastes mentella*) have been documented (Renaud et al. 2012; Hollowed et al. 2013; Fossheim et al. 2015).

The Arctic fish community, including various snail-

CONT. SIDEBAR 5.2: CLIMATE CHANGE IS PUSHING BOREAL FISH NORTHWARD TO THE ARCTIC: THE CASE OF THE BARENTS SEA—M. FOSSHEIM, R. PRIMICERIO, E. JOHANNESEN, R. B. INGVALDSEN, M. M. ASCHAN, AND A. V. DOLGOV

fishes, sculpins, and eel pouts, does not seem to cope well with warming water temperatures (Fossheim et al. 2015). Most of these Arctic fish species are relatively small, stationary, and feed on organisms living on the sea bottom. These species have a more specialized diet than the boreal fish species and are thus more vulnerable to climate change (Kortsch et al. 2015). In addition, they are adapted to life on the shallow shelf of the Barents Sea. Because the central Arctic Ocean is much deeper, it is unlikely that these species will move farther north. However, they can be found farther to the east on the neighboring shelf (e.g., Kara Sea; Fig. SB5.2).

Large fish and marine mammals can move quickly over large distances, while other species, such as small Arctic fish species and organisms that live on or near the seafloor, are more stationary. As a result, two previously separate communities are now mixing together (Fossheim et al. 2015). The larger fish species from the south will compete with the smaller Arctic species for food, and even prey on them directly. Thus, the Arctic community is being pressured from two sides: the marine environment is changing due to rising water temperatures, and new competitors and predators are arriving. It is anticipated that this could result in the local extinction of some Arctic fish species, such as the gelatinous snailfish (*Liparis fabricii*) and even the most abundant Arctic species, the Polar cod (*Boreogadus saida*).

One consequence of the general nature of large boreal fish moving into the Arctic is the development of novel feeding links between incoming and resident species, ultimately changing the configuration of the Arctic marine food web (Kortsch et al. 2015). Arctic food webs contain fewer feeding links than boreal food webs. As cod and other large fish species feeding on many prey move into arctic waters, they establish many new links in the Arctic food web, which becomes more tightly connected. The ecological effects of perturbations will spread faster and more widely in a more interconnected arctic food web, making it more susceptible to environmental stress (Kortsch et al. 2015).

e. *Greenland Ice Sheet*—M. Tedesco, J. E. Box, J. Cappelen, X. Fettweis, K. Hansen, T. Mote, C. J. P. P. Smeets, D. van As, R. S. W. van de Wal, I. Velicogna, and J. Wahr

The Greenland Ice Sheet covers an area of 1.71 million km^2. With a volume of 2.85 million km^3, it is the second largest glacial ice mass on Earth, smaller only than the Antarctic ice sheet. The amount of freshwater stored in the Greenland Ice Sheet has a sea level equivalent of ~7 m. The discharge of the ice to the ocean through runoff and iceberg calving not only increases sea level, but can also alter the ocean thermohaline circulation and global climate (Rahmstorf et al. 2015). Moreover, the high albedo (reflectivity) of the ice sheet surface (together with that of sea ice and snow on land) plays a crucial role in the regional surface energy balance (Tedesco et al. 2011) and the regulation of global air temperatures.

Estimates of the spatial extent of Greenland Ice Sheet surface melting (e.g., Mote 2007; Tedesco 2007; Tedesco et al. 2013) show that in 2015 (Fig. 5.9a) melting occurred over more than half of the ice sheet for the first time since the exceptional melt events of July 2012 (Nghiem et al. 2012). The 2015 melt extent exceeded two standard deviations above the 1981–2010 average, reaching a maximum of 52% of the ice sheet area on 4 July (Fig. 5.9d). By comparison, melt extent in 2014 reached a maximum of 39% of the ice sheet area and ~90% in 2012. A second period of melting, which began in late August, covered between 15% and 20% of the ice sheet (a mean of ~5% over the same period) and lasted until early September. In the summer of 2015 (June–August), the number of melting days along the southwestern and southeastern margins of the ice sheet was close to or below the long-term average, with maximum negative anomalies (i.e., below the 1981–2010 average) of 5–10 days (Fig 5.9a). In contrast, the number of melt days in the northeastern, western, and northwestern regions was up to 30–40 days above the 1981–2010 average, setting new records in terms of meltwater production and runoff over the northwestern regions.

The surface mass balance measured along the southwestern portion of the ice sheet at the K-transect for September 2014 through September 2015 (van de Wal et al. 2005, 2012) was the third least negative since the beginning of the record in 1990 (Tedesco et al. 2015). This is consistent with the negative melting anomalies along the southwestern portion of the ice sheet (Fig. 5.9a). At all PROMICE network stations (www.promice.dk; Ahlstrøm et al. 2008; van As et al. 2011) summer 2015 ablation was low with respect to the 2011–15 period of record (Fig. 5.9b), except at

the most northerly latitudes (Kronprins Christian Land, KPC, 80°N, 25°W; Thule, THU, 76°N, 68°W), where melt totals were slightly above average. The highest recorded melt in 2015, 5.1 m on the Qassimiut lobe (QAS_L station, 61°N, 47°W), was just over half the record-setting 9.3 m at that site in 2010 (Fausto et al. 2012).

Consistent with the distribution of melt anomalies, measurements at weather stations of the Danish Meteorological Institute (DMI; Cappelen 2015) during spring 2015 indicate that summer average temperature anomalies (relative to the 1981–2010 average) were positive at several northerly stations around the Greenland coastline, with values exceeding one standard deviation at Pituffik (+1.2 °C), Upernavik (+1.2°C) and Danmarkshavn (+0.9°C). In contrast, temperatures in south and southwest Greenland (e.g.,Paamiut, Narsarsuaq, Qaqortoq, and Prins Christian Sund) were 1.5 standard deviations below the 1981–2010 average, with temperature anomalies as much as –2.6°C at Narsarsuaq (Tedesco et al. 2015). These widespread low temperatures are consistent with a strong negative spring temperature anomaly centered over Greenland (see section 5b, Fig. 5.2b). Danmarkshavn also experienced its warmest January on record, with a +7.7°C anomaly. A new record August low temperature of –39.6°C occurred on 28 August at Summit (3216 m a.s.l.).

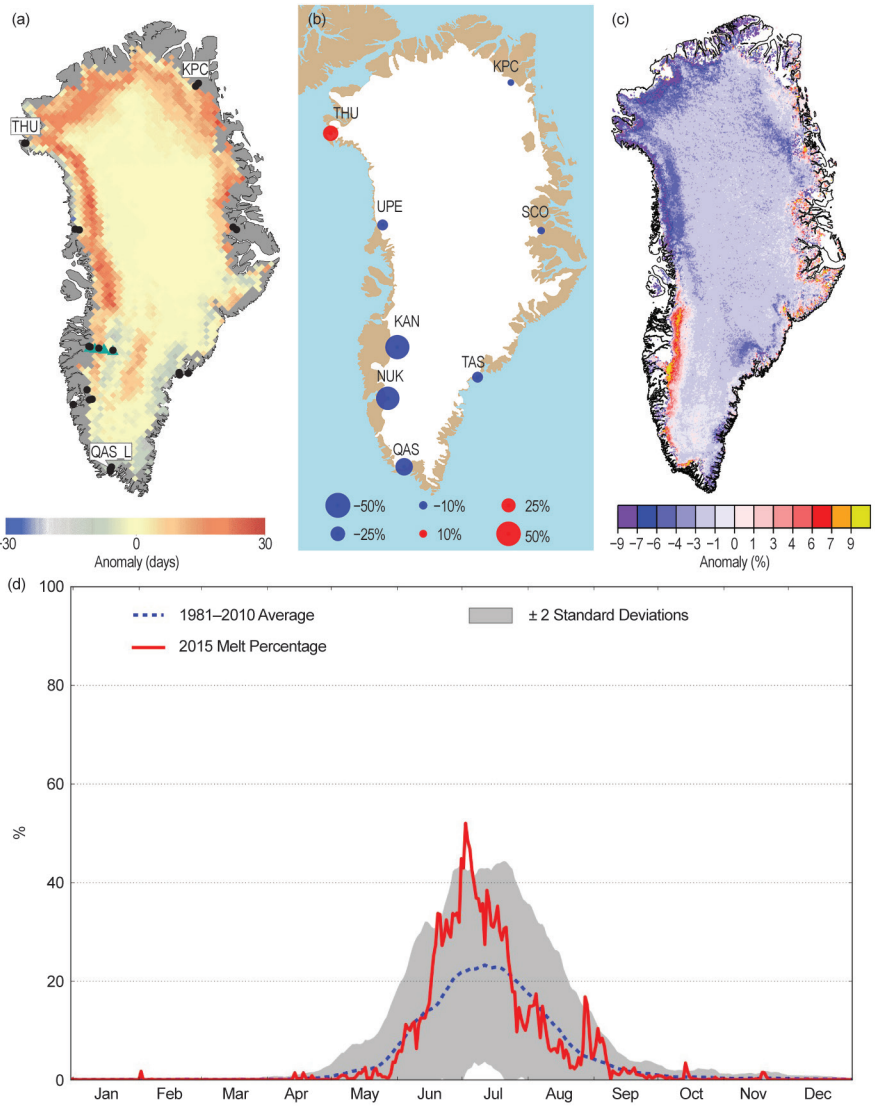

Fig. 5.9. (a) Map of the anomaly (with respect to the 1981–2010 average) of the number of days when melting was detected in summer 2015 using spaceborne passive microwave data. The locations of the stations used for the in situ analysis of surface mass balance and temperature are reported on the map as black disks (PROMICE) and cyan triangles (K-transect). (b) Summer 2015 ablation at PROMICE stations with respect to the 2011–15 period of record. (c) Greenland Ice Sheet surface albedo anomaly for JJA 2015 relative to the average for those months between 2000 and 2009 derived from MODIS data. (d) Daily spatial extent of melting from Special Sensor Microwave Imager/Sounder (SSMIS) as a percentage of the total ice sheet area for all of 2015. The 1981–2010 average spatial extent of melting (dashed line) and ±2 std. dev. of the mean (shaded) are also plotted for reference.

The average albedo for the Greenland Ice Sheet in summer 2015, derived from data collected by the Moderate-resolution Imaging Spectroradiometer (MODIS, after Box et al. 2012), was below the 2000–09 average over the northwestern region and above the average in the southwest (Fig. 5.9c), consistent with the negative surface mass balance and melting day anomalies measured over the same region (Fig. 5.9a). The trend of mean summer albedo over the entire ice sheet for the period 2000–15 remained negative and was estimated to be –5.5% ± 0.4%. In July 2015, when extensive melting occurred (Fig. 5.9d), albedo

averaged over the entire ice sheet was 68%. Albedo in July 2015 was as much as 15%–20% below average along the northwestern ice sheet and along the west coast, where a large increase in melting days was observed in 2015. Over the entire summer, however, the albedo anomaly along the southwestern ice sheet margin coast was positive, consistent with a relatively shorter melt season and with the presence of summer snow accumulation.

GRACE satellite data (Velicogna et al. 2014) are used to estimate monthly changes in the total mass of the Greenland Ice Sheet, including mass gain due to accumulation and summer losses due to runoff and calving (Fig. 5.10). Between the beginning of September 2014 and the beginning of September 2015 GRACE recorded a 174 ± 45 Gt (Gt ≡ 10^9 tons) mass loss, versus an average September-to-September loss of 278 ± 35 Gt for the 2002–15 period. As a comparison, the 2013–14 September-to-September loss was 236 ± 45 Gt (7% of the total loss of ~ 3500 Gt since the beginning of the GRACE record in 2002) and that for 2011–12 was 638 ± 45 Gt (18% of the total loss). The relatively modest loss for the 2014–15 period is consistent with reduced melting over the southwest portion of the ice sheet and increased summer snowfall.

Glacier front classification in LANDSAT and ASTER imagery (after Jensen et al. 2016) reveals that 45 of the widest and fastest flowing marine-terminating glaciers retreated at a slower rate in 2013–15 than in the 1999–2012 period (Fig. 5.11). Between the end of the 2014 melt season and the end of the 2015 melt season, 22 of the 45 glaciers retreated, but the advance of 9 relatively wide glaciers resulted in the lowest annual net area loss in the 16-year period of observations (1999–2015), being –16.5 km² or 7.7 times lower than the annual average area change trend of –127 km² yr^{-1} (Fig. 5.11). Specifically, Petermann Glacier advanced by 0.68 km across a width of 17.35 km, and Kangerdlugssuaq Glacier advanced by 1.68 km across a width of 6.01 km.

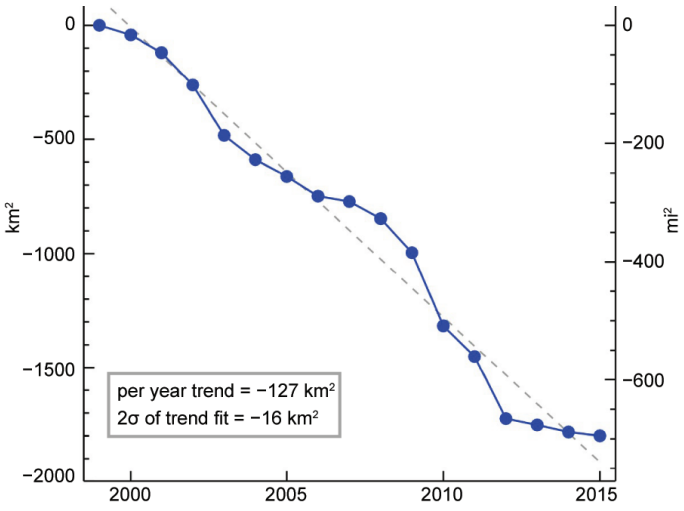

Fig. 5.11. Cumulative net area change (km², left *y*-axis and square miles, right *y*-axis) of 45 of the widest and fastest-flowing marine-terminating glaciers of the Greenland Ice Sheet (Box and Hansen 2015; Jensen et al. 2016). The linear regression is dashed.

f. Glaciers and ice caps outside Greenland—G. Wolken, M. Sharp, L. M Andreassen, A. Arendt, D. Burgess, J. G. Cogley, L. Copland, J. Kohler, S. O'Neel, M. Pelto, L. Thomson, and B. Wouters

Mountain glaciers and ice caps cover an area of over 400 000 km² in the Arctic and are a leading contributor to global sea level change (Gardner et al. 2011, 2013; Jacob et al. 2012). They gain mass by snow accumulation and lose mass by surface melt runoff, and by iceberg calving where they terminate in water (ocean or lake). The total mass balance (ΔM) is defined as the difference between annual snow accumulation and annual mass losses (by iceberg calving plus surface melt runoff). Of the 27 glaciers currently monitored, however, only three (Kongsvegen, Hansbreen, and Devon Ice Cap NW) lose any mass by iceberg calving into the ocean. For all glaciers discussed here, the climatic mass balance is reported (B_{clim}, the difference between annual snow accumulation and annual runoff). B_{clim} is a widely used index of how glaciers respond to climate variability and change.

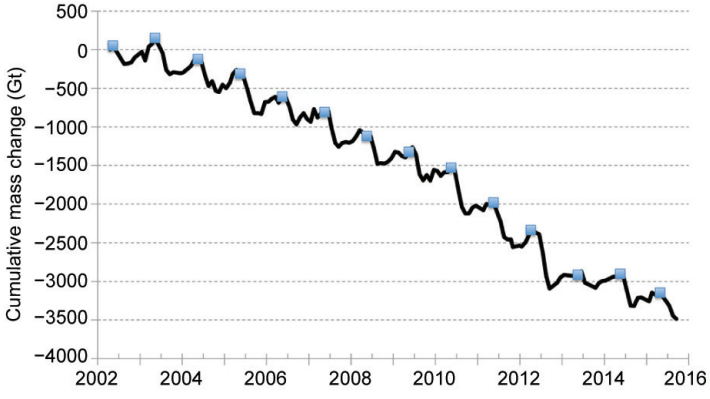

Fig. 5.10. Cumulative change in the total mass (Gt) of the Greenland Ice Sheet between Apr 2002 and Sep 2015 estimated from GRACE measurements. The square symbols denote Apr values for reference.

B_{clim} measurements for mass balance year 2014/15 are available for only 9 of the 26 glaciers that are monitored across the Arctic (three each in Alaska and Svalbard, and one in Norway), and some of these are still provisional. Therefore, we focus on the 2013/14 B_{clim} measurements, which are available for 21 glaciers (WGMS 2015b). These glaciers are located in Alaska (three), Arctic Canada (four), Iceland (seven), Svalbard (three), Norway (three), and Sweden (one; Fig. 5.12; Table 5.1). For these glaciers as a group, the mean B_{clim} in 2013/14 was negative. However, five glaciers [one each in Arctic Canada (Meighen Ice Cap) and Iceland (Dyngjujökull) and three in Svalbard (Midre Lovenbreen, Austre Broggerbreen, and Kongsvegen)] had positive balances.

For the Arctic as a whole, 2013/14 was the 17th most negative mass balance year on record (the first record dates from 1946) and the 12th most negative year since 1989 (i.e., the median for the 25-year period), when annual measurements of at least 20 glaciers began. This balance year continues the increasingly negative trend of cumulative regional climatic mass balances, calculated by summing the annual mean mass balances for all glaciers in each reporting region of the Arctic (Fig. 5.13). For Svalbard, 2013/14 was among the least negative mass balance years on record, and the climatic balances of each of its three glaciers were among the 3–9 most positive since 1987. Local meteorological observations suggest that the positive balances in Svalbard were attributable to high winter (October–May) precipitation, especially at low elevations, that was followed by a relatively cool summer (June–August). Melt suppression over Svalbard, as well as the Russian Arctic Archipelagos and the northernmost islands of Arctic Canada, was likely linked to negative 850-hPa air temperature anomalies in June–September. In contrast, in 2013/14 the mean measured climatic balance of glaciers in Alaska was the fifth most negative since 1966, with Lemon Creek and Wolverine glaciers registering their third and fourth most negative years on record, respectively. The negative balances of Alaska, Iceland, and northern Scandinavia glaciers in 2013/14 were most likely linked to melt increases caused by positive air temperature anomalies at the 850-hPa level in July–September that exceeded +2.5°C in northern Norway and Sweden (data from NCEP–NCAR reanalysis). Indeed, in 2014, many locations in northern Scandinavia reported their highest summer air temperatures since records began (Overland et al. 2015).

Among the nine glaciers for which 2014/15 B_{clim} measurements have been reported, the balances of glaciers in Alaska, Svalbard, and northern Norway

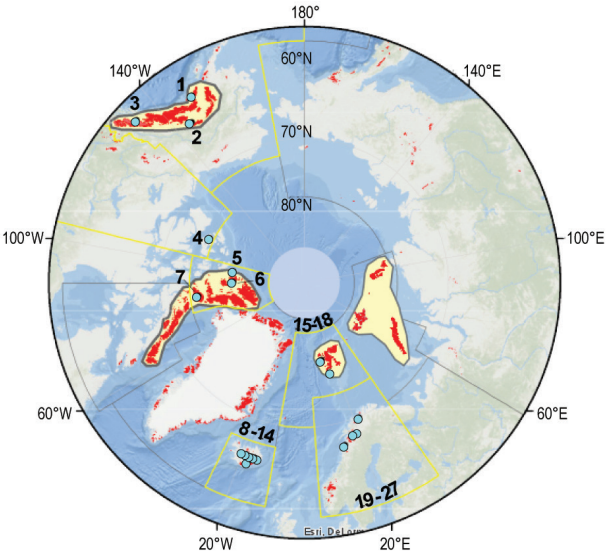

Fig. 5.12. Locations (green circles) of 27 Arctic glaciers with long-term records of annual climatic mass balance (B_{clim}). See Table 5.1 for glacier names. Regions outlined in yellow are the Randolph Glacier Inventory (RGI) regions of the Arctic (Pfeffer et al. 2014). In regions where individual glaciers are located too close together to be identifiable on the map, their numbers are shown at the edge of the RGI region in which they occur. Red shading indicates glaciers and ice caps, including ice caps in Greenland outside the ice sheet. Yellow shading shows the solution domains for regional mass balance estimates for Alaska, Arctic Canada, Russian Arctic, and Svalbard derived using gravity data from the GRACE satellites (see Fig. 5.3).

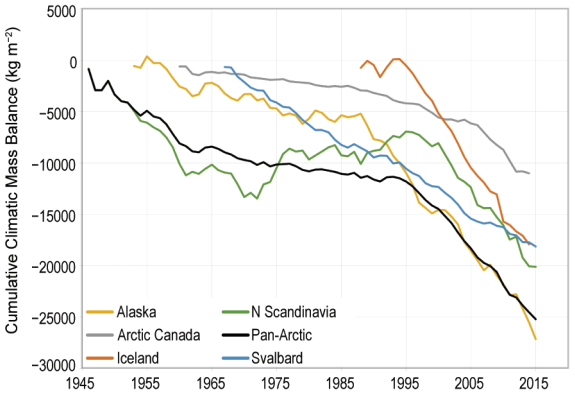

Fig. 5.13. Cumulative climatic mass balances (B_{clim} in kg m^{-2}) for glaciers in five regions of the Arctic and for the Arctic as a whole (Pan–Arctic). Mean balances are calculated for glaciers monitored in each region in each year and these means are summed over the period of record. Note that the period of monitoring varies between regions and that the number and identity of glaciers monitored in a given region may vary between years.

Table 5.1. Measured annual climatic mass balance (B_{clim}) of glaciers in Alaska, the Canadian Arctic, Iceland, Svalbard, and northern Scandinavia for 2013/14 and 2014/15, along with the 1980–2010 mean and standard deviation for each glacier (column 3). Mass balance data are from the World Glacier Monitoring Service (2015; 2016), with corrections to Svalbard data provided by J. Kohler and to Alaska data provided by S. O'Neel, and with updates from the Norwegian Water Resources and Energy Directorate (NVE) database. Numbers in column 1 identify glacier locations in Fig. 5.1. Note that 2014/15 results may be based upon data collected before the end of the 2015 melt season and may be subject to revision.

Region	Glacier (Record length, years)	Mean Climatic Balance 1980–2010 (kg m^{-2} yr^{-1})	Standard Deviation of Climatic Mass Balance 1980–2010 (kg m^{-2} yr^{-1})	Climatic Balance 2013/14 (kg m^{-2} yr^{-1})	Climatic Balance 2014/15 (kg m^{-2} yr^{-1})
Alaska					
1	Wolverine (50)	−285	1205	−1950	−1130
3	Lemon Creek (63)	−584	709	−1825	−2270
2	Gulkana (50)	−505	738	−220	−1440
Arctic Canada					
7	Devon Ice Cap (54)	−153	176	−246	
5	Meighen Ice Cap (53)	−173	284	+57	
4	Melville South Ice Cap (52)	−295	369	−159	
6	White (52)	−239	260	−417	
Iceland					
8	Langjökull S. Dome (18)	−1448	817	−1950	
9	Hofsjökull E (24)	−602	1009	−990	
9	Hofsjökull N (25)	−606	787	−950	
9	Hofsjökull SW (24)	−978	947	−990	
14	Köldukvislarjökull (22)	−529	738	−887	
10	Tungnaarjökull (23)	−1170	873	−1535	
13	Dyngjujökull (17)	−133	912	+170	
12	Brúarjökull (22)	−367	660	−34	
11	Eyjabakkajökull (23)	−867	813	−353	
Svalbard					
17	Midre Lovenbreen (48)	−356	305	+30	−450
16	Austre Broggerbreen (49)	−469	342	+10	−610
15	Kongsvegen (29)	−70	378	+140	−160
18	Hansbreen (26)	−431	512	−227	
Nortern Scandinavia					
20	Engabreen (45)	+463	1091	−892	+668
21	Langfjordjøkelen (25)	−927	781	−780	−800
22	Marmaglaciaren (23)	−430	525		
23	Rabots Glaciar (29)	−394	560		
24	Riukojietna (26)	−592	805		
25	Storglaciaren (68)	−113	698	−890	
26	Tarfalaglaciaren (18)	−212	1101		
27	Rundvassbreen (8)	−777		−790	−20

(Langfjordjøkelen) were negative, while those of glaciers in central Norway were near balance (Rundvassbreen) or positive (Engabreen). The pattern of negative balances in Alaska and Svalbard is also captured in time series of regional total stored water estimates (Fig. 5.14), derived using GRACE satellite gravimetry available since 2003. Annual storage changes are proxy for changes in the regional annual glacier mass balance (ΔM) for the heavily glacierized regions of the Arctic (Luthcke et al. 2013). Measurements of ΔM in 2014/15 for all the glaciers and ice caps in Arctic Canada and the Russian Arctic also

show a negative mass balance year. The GRACE-derived time series clearly show a continuation of negative trends in ΔM for all measured regions in the Arctic. These measurements of B_{clim} and ΔM are consistent with anomalously warm (up to +1.5°C) June–August air temperatures over Alaska, Arctic Canada, the Russian Arctic, and Svalbard in 2015 (section 5b), and anomalously cool temperatures in northern Scandinavia, particularly in June and July (up to –2°C).

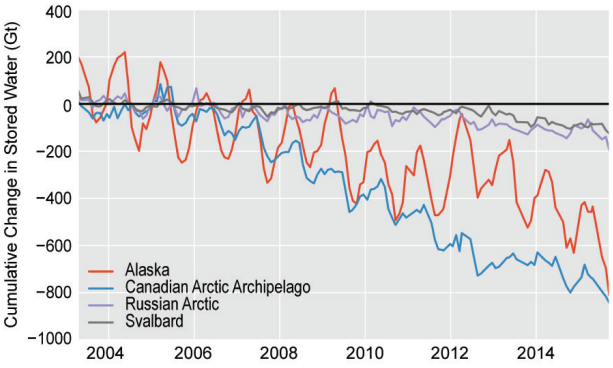

Fig. 5.14. Cumulative changes in regional total stored water for 2003–15 (Gt), derived using GRACE satellite gravimetry. Annual storage changes are proxy for changes in the regional annual glacier mass balance (ΔM). The estimated uncertainty in regional mass changes is 10 Gt yr^{-1} for the Gulf of Alaska, 8 Gt yr^{-1} for the Canadian Arctic, 8 Gt yr^{-1} for the Russian Arctic, and 4 Gt yr^{-1} for Svalbard. These errors include the formal error of the least squares fit and the uncertainties in the corrections for glacial isostatic adjustment, Little Ice Age, and terrestrial hydrology.

g. Terrestrial snow cover—C. Derksen, R. Brown, L. Mudryk, and K. Luojus

The Arctic (land areas north of 60°N) is always completely snow-covered in winter and almost snow free in summer, so the transition seasons of autumn and spring are significant when characterizing variability and change. The timing of spring snowmelt is particularly significant because the transition from highly reflective snow cover to the low albedo of snow-free ground is coupled with increasing solar radiation during the lengthening days of the high-latitude spring. The 2015 spring melt season provided continued evidence of earlier snowmelt across the terrestrial Arctic. There is increased awareness of the impact of these changes on the Arctic climate system, the freshwater budget, other components of the cryosphere (such as permafrost and associated geochemical cycles), and Arctic ecosystems (Callaghan et al. 2011).

Snow cover extent (SCE) anomalies (relative to the 1981–2010 reference period) for the 2015 Arctic spring (April, May, June) were computed separately for the North American and Eurasian sectors of the Arctic from the NOAA snow chart Climate Data Record, maintained at Rutgers University (Estilow et al. 2015; http://climate.rutgers.edu/snowcover/). Consistent with nearly all spring seasons of the past decade, both May and June SCE anomalies were strongly negative in 2015 (Fig. 5.15); June SCE in both the North American and Eurasian sectors of the Arctic was the second lowest in the snow chart record, which extends back to 1967.

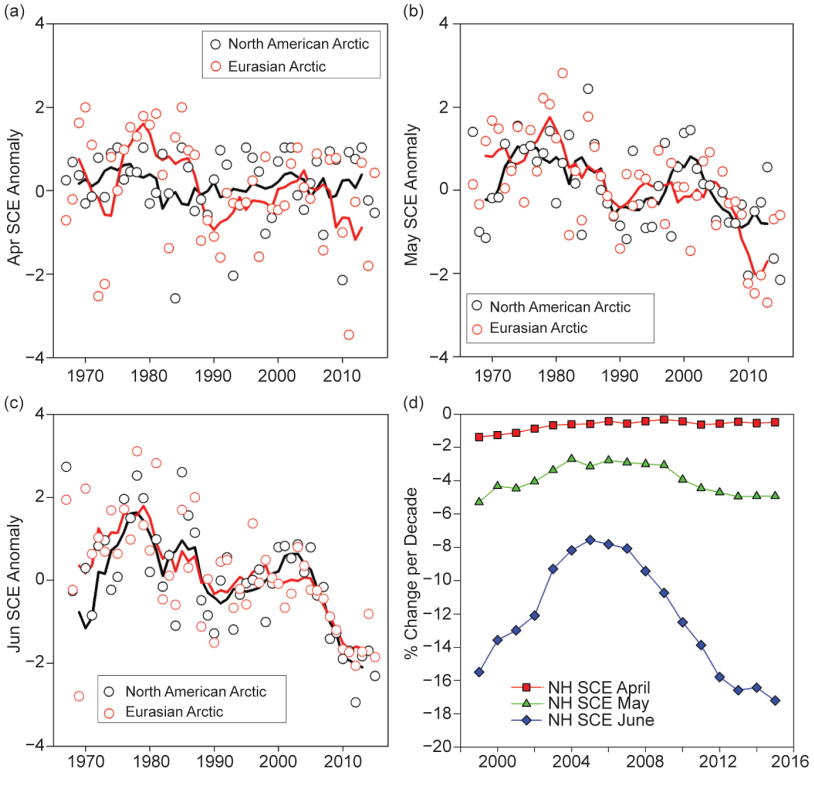

Fig. 5.15. Monthly Arctic snow cover extent standardized (and thus unitless) anomaly time series (with respect to 1981–2010) from the NOAA snow chart Climate Data Record for (a) Apr, (b) May, and (c) Jun 1967–2015 (solid lines denote 5-yr moving average); (d) % change decade^{-1} in spring snow cover extent for running time series starting in 1979 (1979–98, 1979–99, 1979–2000, etc.).

For the fifth time in the past six years (2010–15), Arctic SCE in June was below 3 million km^2 despite never falling below this threshold in the previous 43 years of the snow chart data record (1967–2008). Figure 5.15d shows the changing rate of SCE loss across the Arctic since 1998 via calculations over running time periods since 1979, the first year of the satellite passive microwave record used to track sea ice extent. The April and May SCE reductions have remained relatively consistent year over year, ranging between –1% and –2% decade^{-1} (April; insignificant at 95%) and –3% and –5% per decade^{-1} (May; significant at 99%). A significant rate of June SCE loss was identified over the first 20 years (nearly –16% for 1979–98) due to rapid reductions in the 1980s, which then plateaued due to a period of stable spring snow cover during the 1990s. Since 2005, the rate of June SCE loss has increased again, reaching almost 18% decade^{-1} for the period 1979–2015 (compared to the 1981–2010 mean June SCE). Since 2011, the rate of June snow cover loss has exceeded the much publicized rate of September sea ice loss (section 5c).

There are complex interactions between regional variability in the onset of snow cover in the autumn, subsequent winter season snow accumulation patterns (which themselves are driven by the complex interplay of temperature and precipitation anomalies), and continental-scale spring SCE anomalies (shown in Fig. 5.15). Snow cover duration (SCD) departures (relative to the 1998–2010 period) derived from the NOAA daily Interactive Multi-sensor Snow and Ice Mapping System (IMS) snow cover product (Helfrich et al. 2007) suggest earlier snow cover onset in the autumn over much of the Arctic for the 2014/15 snow year (Fig. 5.16a). This is consistent with premelt April snow depth anomalies (relative to the 1999–2010 average), derived from the Canadian Meteorological Centre (CMC) daily gridded global snow depth analysis (Brasnett 1999), which were largely positive over much of the Arctic land surface (25.1% and 33.7%, respectively, for the North American and Eurasian sectors of the Arctic). There was a notable east–west snow depth gradient across Eurasia in April 2015 with above-average snow depth in eastern Siberia and below-average snow depth across western Siberia and northern Europe. The North American Arctic was characterized by a more latitudinal gradient of deeper-than-normal snow depth north of the boreal tree line and shallower-than-normal snow depth across the boreal forest. Note that the CMC results shown in Figs. 5.17a–c mask out anomalies over high elevation areas (in the Canadian Arctic Archipelago, Baffin Island, coastal Alaska) known to be affected by a bias toward higher winter snow depths since 2006 due to changes in the resolution of the precipitation forcing used as part of the CMC analysis. Strong positive surface temperature anomalies over central Siberia, Alaska, and the western Canadian Arctic in May (which persisted into June; section 5b) were associated with rapid reductions in regional snow depth reflected in the May and June depth anomalies (Figs. 5.17b,c) and earlier than normal snowmelt in these regions (Fig. 5.16b), which drove the negative continental-scale SCE anomalies in May and June (Figs. 5.16b,c).

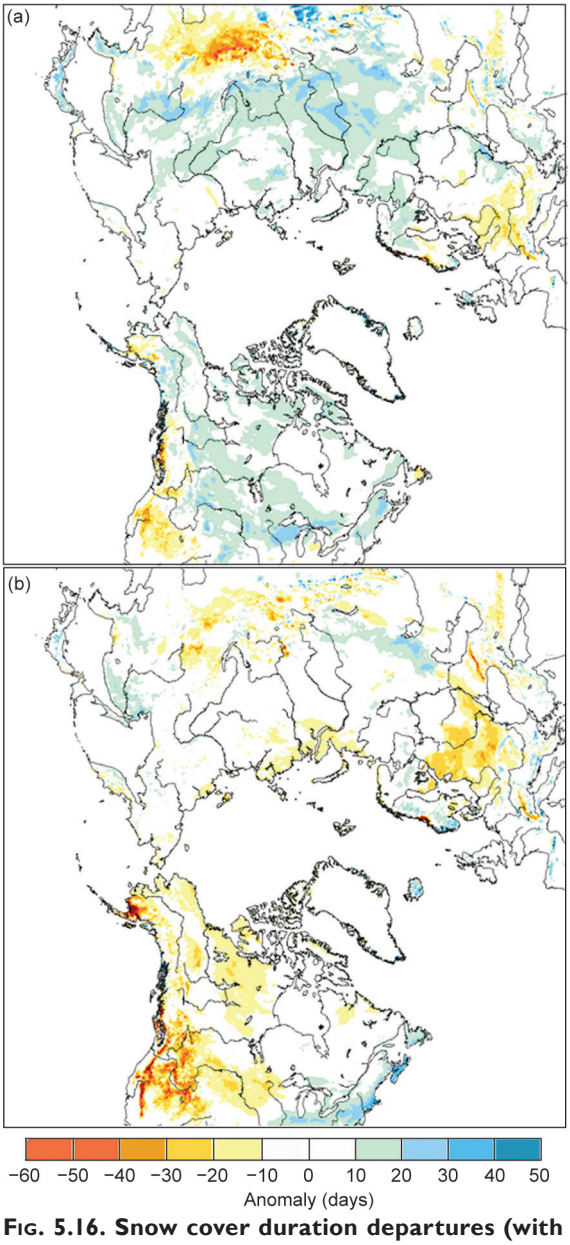

Fig. 5.16. Snow cover duration departures (with respect to 1998–2010) from the NOAA IMS data record for the (a) 2014 autumn season and (b) 2015 spring season.

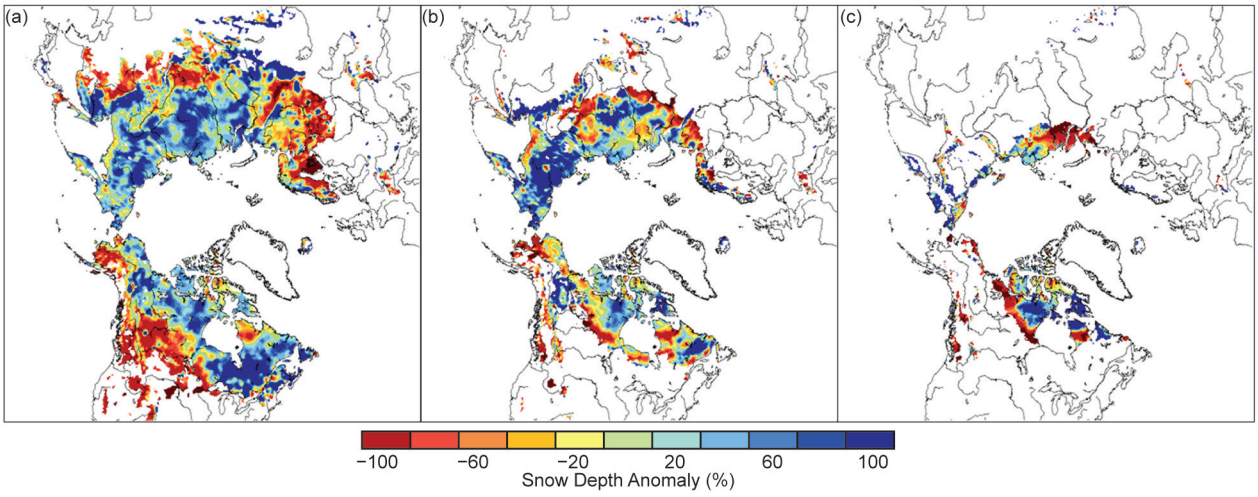

Fig. 5.17. Snow depth anomaly (% of 1999–2010 average) from the CMC snow depth analysis for (a) Apr, (b) May, and (c) Jun 2015.

h. River discharge—R. M. Holmes, A. I. Shiklomanov, S. E. Tank, J. W. McClelland, and M. Tretiakov

River discharge integrates hydrologic processes occurring throughout the surrounding landscape. Consequently, changes in the discharge of large rivers can be a sensitive indicator of widespread changes in watersheds (Rawlins et al. 2010; Holmes et al. 2013). Changes in river discharge also impact coastal and ocean chemistry, biology, and circulation. This interaction is particularly strong in the Arctic, given the relative volume of river discharge to ocean volume. Rivers in this region transport >10% of the global river discharge into the Arctic Ocean, which represents only ~1% of the global ocean volume (Aagaard and Carmack 1989; McClelland et al. 2012).

In this section, annual river discharge values since 2011 are presented for the eight largest Arctic rivers, and recent observations are compared to a 1980–89 reference period (the first decade with data from all eight rivers). Six of the rivers lie in Eurasia and two are in North America. Together, the watersheds of these rivers cover 70% of the 16.8×10^6 km^2 pan-Arctic drainage area and, as such, account for the majority of riverine freshwater inputs to the Arctic Ocean (Fig. 5.18). Discharge data for the six Eurasian rivers are analyzed through 2015, whereas data from the Yukon and Mackenzie Rivers in North America are only available through 2014. Most of these data are now available through the Arctic Great Rivers Observatory (www.arcticgreatrivers.org).

A long-term increase in Arctic river discharge has been well documented and may be linked to increasing precipitation associated with global warming (Peterson et al. 2002; McClelland et al. 2006; Shiklomanov and Lammers 2009; Overeem and Syvitski 2010; Rawlins et al. 2010). The long-term discharge trend is greatest for rivers of the Eurasian Arctic and constitutes the strongest evidence of intensification of the Arctic freshwater cycle (Rawlins et al. 2010).

In 2015, the combined discharge of 2051 km^3 for the six largest Eurasian Arctic rivers was 15% greater than the 1980–89 average (Fig. 5.19; Table 5.2), and the peak discharge occurred earlier than the average over the same period (Fig. 5.20). This is the fourth highest combined discharge value since measurements began in 1936. The four highest values have

Fig. 5.18. Map showing the watersheds of the eight rivers featured in this section. The blue dots show the location of the discharge monitoring stations and the red line shows the boundary of the pan-Arctic watershed.

Table 5.2. Annual discharge for 2012, 2013, and 2014 for the eight largest Arctic rivers, compared to long-term and decadal averages back to the start of observations. Values for 2015 are provided for the six Eurasian rivers. Red values indicate provisional data, which are subject to modification before official data are released.

Discharge (km^3 yr^{-1})									
	Yukon	Mackenzie	Pechora	S. Dvina	Ob'	Yenisey	Lena	Kolyma	Sum
2015			123	80	527	654	585	82	
2014	227	272	116	91	448	640	607	86	2487
2013	213	311	82	97	372	527	600	80	2282
2012	232	306	103	117	300	458	665	59	2240
Average 2010–15	212	293	108	93	409	594	583	75	2366
Average 2000–09	207	305	124	103	415	640	603	78	2475
Average 1990–99	217	275	117	111	405	613	532	68	2338
Average 1980–89	206	273	108	100	376	582	549	68	2262
Average 1970–79	184	292	108	94	441	591	529	65	2304
Average 1960–69		273	112	98	376	546	535	73	
Average 1950–59			110	108	380	566	511	74	
Average 1940–49			102	100	424	578	498	72	
Average for Period of Record	206	286	111	100	401	589	540	71	2305

all occurred in the past 14 years. Overall, the most recent data indicate a continuing long-term increase in Eurasian Arctic river discharge, at a rate of 3.5% ± 2.1% $decade^{-1}$ since 1976. Looking more closely at recent years, Eurasian Arctic river discharge generally declined between 2007 and 2012 and then began to increase again in 2013. Values for 2012 (1702 km^3), 2013 (1759 km^3), and 2014 (1989 km^3) were 5% less, 1% less, and 2% greater than the 1980–89 period, respectively. The short-term variability in Eurasian Arctic river discharge is consistent with previous increases and decreases over 4–6 year intervals in the past (Fig. 5.19).

For the North American Arctic rivers considered here (Yukon and Mackenzie), the combined discharge declined each year from 2012 (538 km^3) to 2014 (499 km^3), yet in each of those years the combined discharge was greater than the long-term average (493 km^3 $year^{-1}$; Fig. 5.19; Table 5.2). Thus, as discussed for Eurasian rivers, these most recent data indicate a longer-term pattern of increasing river discharge (Fig. 5.19). At a rate of 2.6% ± 1.7% $decade^{-1}$ since 1976, the overall trends of increasing discharge are remarkably similar for the North American and Eurasian rivers. (Increases per decade follow a Mann – Kendall trend analysis; error bounds are 95% confidence intervals for the trend.)

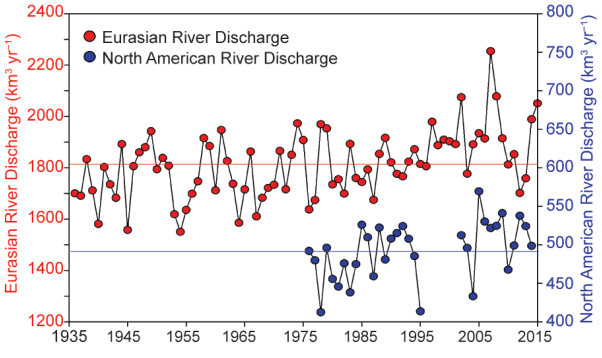

Fig. 5.19. Long-term trends in annual discharge for Eurasian and North American Arctic rivers. The Eurasian rivers are Severnaya Dvina, Pechora, Ob', Yenisey, Lena, and Kolyma. The North American rivers are Yukon and Mackenzie. Note the different scales for the Eurasian and North American river discharge; discharge from the former is 3–4 times greater than the latter. Reference lines show long-term means for the Eurasian (1812 km^3 yr^{-1}, 1936–2015) and North American (493 km^3 yr^{-1}, 1976–2014) rivers.

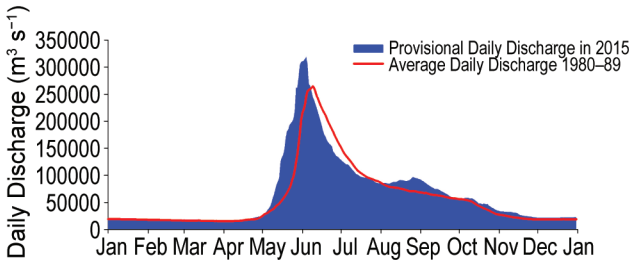

Fig. 5.20. Combined daily discharge for the six Eurasian Arctic rivers in 2015 compared to the 1980–89 average.

Considering the eight Eurasian and North American Arctic rivers together, their combined discharge in 2014 (2487 km^3) was 10% greater than the average discharge for 1980–89. Comparing 2014 to 2012, the combined discharge of these eight rivers was almost 250 km^3 greater in 2014. For perspective, 250 km^3 is approximately 14 times the annual discharge of the Hudson River, the largest river on the east coast of the United States.

i. Terrestrial permafrost—V. E. Romanovsky, S. L. Smith, K. Isaksen, N. I. Shiklomanov, D. A. Streletskiy, A. L. Kholodov, H. H. Christiansen, D. S. Drozdov, G. V. Malkova, and S. S. Marchenko

Permafrost is defined as soil, rock, and any other subsurface earth material that exists at or below 0°C continuously for two or more consecutive years. On top of permafrost is the active layer, which thaws during the summer and freezes again the following winter. The mean annual temperature of permafrost and the active layer thickness (ALT) are good indicators of changing climate and therefore designated as essential climate variables (Smith and Brown 2009; Biskaborn et al. 2015) by the Global Climate Observing System Program of the World Meteorological Organization. Changes in permafrost temperatures and ALT at undisturbed locations in Alaska, Canada, Russia, and the Nordic region (Fig. 5.21) are reported here. Regional variability in permafrost temperature records, described below, indicates more substantial permafrost warming since 2000 in higher latitudes than in the subarctic. This is in general agreement with the pattern of average air temperature anomalies.

In 2015, record high temperatures at 20-m depth were measured at all permafrost observatories on the North Slope of Alaska (Barrow, West Dock, Franklin Bluffs, Happy Valley, and Galbraith Lake in Fig. 5.22a; Romanovsky et al. 2015). The permafrost temperature increase in 2015 was substantial and comparable to the highest rate of warming observed in this region so far, which occurred during the period 1995–2000; 20-m depth temperatures in 2015 were from 0.10°C to 0.17°C higher than those in 2014 (Fig. 5.22a) on the North Slope. Since 2000, temperature at 20-m depth in this region has increased between 0.21°C and 0.66°C decade^{-1} (Fig. 5.22a; Table 5.3). Permafrost temperatures in Interior Alaska were higher in 2015 than 2014 at all sites (Old Man, College Peat, Birch Lake, Gulkana, and Healy in Fig. 5.22b), except for Coldfoot. Notably, this warming followed slight cooling of 2007–13 (Fig. 5.22b). However, the recent warming in the interior (see section 5b; Fig. 5.2) was not strong enough to bring permafrost temperatures back to the record highs observed between the mid-1990s and the mid-2000s except at Gulkana (Fig. 5.22b; Table 5.3).

In northwestern Canada, temperatures in warm permafrost of the central Mackenzie Valley (Norman Wells and Wrigley in Fig. 5.22b) were similar in 2014/15 to those observed the previous year.

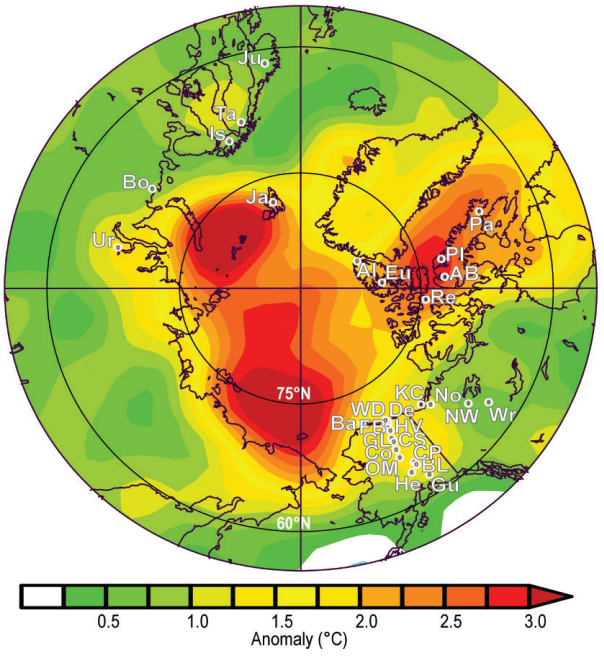

Fig. 5.21. Location of the permafrost monitoring sites shown in Fig. 5.22 superimposed on average air temperature anomalies during 2000–14 (with respect to the 1971–2000 mean) from the NCEP–NCAR reanalysis (Kalnay et al. 1996) (Source: NOAA/ESRL.) Sites shown in Fig. 5.22 are (a) Barrow (Ba), West Dock (WD), KC-07 (KC), Deadhorse (De), Franklin Bluffs (FB), Galbraith Lake (GL), Happy Valley (HV), Norris Ck (No); (b) College Peat (CP), Old Man (OM), Chandalar Shelf (CS), Birch Lake (BL), Coldfoot (Co), Norman Wells (NW), Wrigley 2 (Wr), Healy (He), Gulakana (Gu), Wrigley 1 (Wr); (c) Eureka EUK4 (Eu), Alert BH2 (Al), Alert BH5 (Al), Resolute (Re), Alert BH1 (Al), Arctic Bay (AB), Pond Inlet (PI), Pangnirtung (Pa); (d) Janssonhaugen (Ja), Urengoy #15-10 (Ur), Juvvasshøe (Ju), Tarfalaryggen (Ta), Bolvansky #59 (Bo), Bolvansky #65 (Bo), Urengoy #15-06 (Ur), Bolvansky #56 (Bo), Iskoras Is-B-2 (Is).

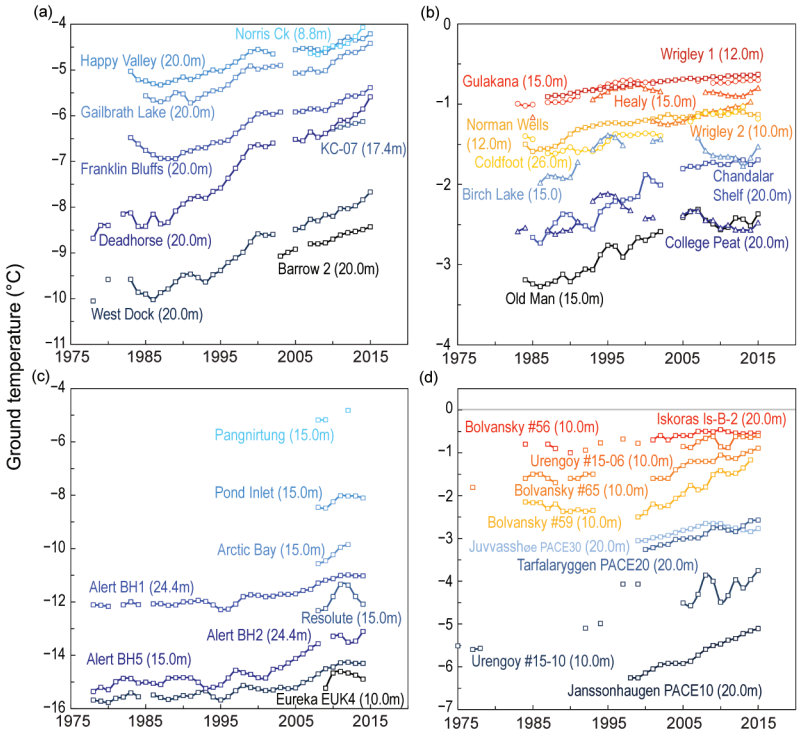

Fig. 5.22. Time series of mean annual ground temperature at depths of 9–26 m below the surface at selected measurement sites that fall roughly into the Adaptation Actions for a Changing Arctic Project (AMAP 2015) priority regions: (a) cold continuous permafrost of NW North America (Beaufort–Chukchi region); (b) discontinuous permafrost in Alaska and northwestern Canada; (c) cold continuous permafrost of eastern and high Arctic Canada (Baffin Davis Strait); (d) continuous to discontinuous permafrost in Scandinavia, Svalbard, and Russia/Siberia (Barents region). Temperatures are measured at or near the depth of penetration of the seasonal ground temperature variations. Data series are updated from Christiansen et al. 2010; Romanovksy et al. 2015; Smith et al. 2015; Ednie and Smith 2015.

Table 5.3. Change in mean annual ground temperature (MAGT; °C decade^{-1}) for sites shown in Fig. 5.22, for which data are available for 2015 († indicates discontinuous permafrost regions). For sites with records initiated prior to 2000, the rate for the entire available record is provided along with the rate for the period after 2000. (Note records for some sites only began after 2007 as shown in Fig. 5.22).

Region	Sites	Entire Record	Since 2000
Central Mackenzie Valley †	Norman Wells (NW), Wrigley (Wr)	+0.1 to +0.2	<+0.1 to +0.2
Northern Mackenzie Valley	Norris Ck (No), KC-07(KC)	NA	+0.4 to +0.7
Baffin Island	Pond Inlet (PI)	NA	+0.7
High Canadian Arctic	Resolute (Re), Eureka (Eu)	NA	+0.4 to +0.7
High Canadian Arctic	Alert (Al), BH5, BH1, BH2	+0.53, +0.3 to +0.4	+1.2, +0.7 to +0.9
Alaskan Arctic plain	West Dock (WD), Deadhorse (De), Franklin Bluffs (FB), Barrow (Ba)	+0.33 to +0.81	+0.36 to +0.66
Northern foothills of the Brooks Range, Alaska	Happy Valley (HV), Galbraith Lake (GL)	+0.25 to +0.37	+0.21 to +0.35
Southern foothills of the Brooks Range, Alaska †	Coldfoot (Co), Chandalar Shelf (CS), Old Man (OM)	+0.07 to +0.31	+0.13 to +0.18
Interior Alaska †	College Peat (CP), Birch Lake (BL), Gulkana (Gu), Healy (He)	+0.03 to +0.15	–0.05 to +0.02
North of West Siberia	Urengoy 15-06 and 15-10 (Ur)	+0.31 to +0.47	+0.1 to +0.19
Russian European North	Bolvansky 56, 59, and 65 (Bo)	+0.18 to +0.46	+0.1 to +0.83
Svalbard	Janssonhaugen (Ja)	+0.7	+0.7
Northern Scandinavia †	Tarfalarggen (Ta), Iskoras Is-B-2 (Is)	NA	+0.1 to +0.4
Southern Norway †	Juvvasshøe (Ju)	+0.2	+0.2

Permafrost in this region has generally warmed since the mid-1980s, with less warming observed since 2000 (Table 5.3), corresponding to a period of steady air temperatures. In contrast, greater recent warming has been observed in the colder permafrost of the northern Mackenzie (Norris Ck, KC-07 in Fig. 5.22a and Table 5.3) with 2014/15 temperatures higher than those recorded over the previous 5–7 years, reflecting an increase in air temperatures over the last decade (Fig. 5.21).

Mean temperatures for 2014/15 in the upper 25 m of the ground at Alert, northernmost Ellesmere Island in the high Canadian Arctic, were among the highest recorded since 1978 (Fig. 5.22c). Since 2010, temperatures have changed little or even declined, consistent with lower air temperatures since 2010 (Smith et al. 2015). However, higher permafrost temperature at 15-m depth in 2014/15 compared to 2013/14 appears to reflect an increase in air temperature since 2013. Since 2000, Alert permafrost temperatures have increased at a higher rate (Table 5.3) than that for the entire record (Smith et al. 2015), consistent with air temperature anomaly patterns (Fig. 5.21). Short records, from other high Arctic sites in the Queen Elizabeth Islands (Resolute and Eureka) and on Baffin Island (Pond Inlet) in the eastern Arctic, indicate some cooling of permafrost since 2012/13 at 10–15-m depth (Fig. 5.22c). However, a general warming trend is observed (Table 5.3) with higher temperatures in 2014/15 than in 2008/09 when measurements began.

Similar to northern Alaska and the Canadian high Arctic, permafrost temperature has increased by 1–2°C in northern Russia during the last 30 to 35 years. In the Russian European North and in the western Siberian Arctic, for example, temperatures at 10-m depth have increased by ~0.4°C to 0.6°C decade^{-1} since the late 1980s at colder permafrost sites (in Fig. 5.22d, Bolvansky #59, Urengoy #15-5, and #15-10). Less warming has been observed at warm permafrost sites (Table 5.3; in Fig. 5.22d, sites Bolvansky #56 and Urengoy #15-6; Drozdov et al. 2015).

In the Nordic countries (including Svalbard), regional warming and thawing of permafrost have been observed recently (Christiansen et al. 2010; Isaksen et al. 2011; Farbrot et al. 2013). Since 2000, temperature at 20-m depth has increased between 0.1°C and 0.7°C decade^{-1} (Fig. 5.22d; Table 5.3) with lower rates of increase occurring at sites in the discontinuous permafrost zone that are affected by latent heat exchange at temperatures close to 0°C. Higher temperature increases occurred at colder permafrost sites on Svalbard and in northern Scandinavia. In southern Norway permafrost was warmer in 2015 compared to 2014, a warming that followed a period of cooling between 2011 and 2014.

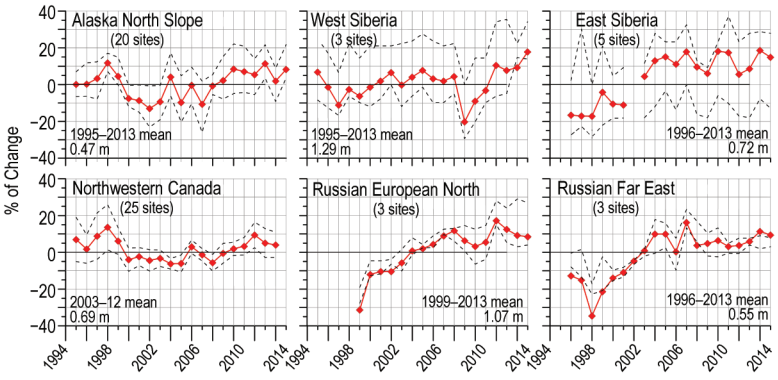

Fig. 5.23. Long-term active-layer change from selected sites in six different Arctic regions as observed by the Circumpolar Active Layer Monitoring project (Shiklomanov et al. 2012). The data are presented as annual percentage deviations from the mean value for the period of observations. Thaw depth observations from the end of the thawing season were used. Only sites with at least 10 years of continuous thaw depth observations are shown in the figure. Solid red lines show mean values. Dashed black lines represent maximum and minimum values. In the Nordic countries (not shown here) active layer records (1996–2015) indicate a general increase in ALT since 1999. Maximum ALT was observed in 2011 followed by a period of thinner active layers.

Active layer thickness [determined by probing according to Brown et al. (2000) and Shiklomanov et al. (2012)] at North Slope and Alaska Interior locations was on average greater in 2015 than in 2014 (Fig. 5.23). An increase in the thickness of the ALT indicates warming surface temperature. Of 26 North Slope sites observed in 2015, only nine had ALT values within 1 cm of those observed in 2014, while the majority of sites had greater ALT values than in 2014. The average ALT in 2015 for the 20 North Slope sites with records of at least 10 years was 0.51 m, which is 3 cm higher than the 1995–2013 average. In the interior of Alaska, three of the four active sites reported an ALT increase in 2015. The most pronounced change occurred at a site where surface cover was burned in 2010. Here ALT was 1.78 m in 2015, which is 0.10 m greater than the 2014 value and 1.23 m greater than the prefire 1990–2010 average.

Records from 25 sites with thaw tubes in the Mackenzie Valley, northwestern Canada, indicate that ALT in 2014 (the most recent year data are available) was

on average about 4% greater than the 2003–12 mean (Fig. 5.23). Although ALT in this region has generally increased since 2008 (Duchesne et al. 2015), there has been a decrease since 2012.

In Russia, active layer observations were conducted at 44 sites in 2015. Since 2009, a progressive increase in ALT is evident for western Siberian locations (Fig. 5.23), with a substantial increase in 2015 of 0.05–0.20 m. Locations in the Russian European North have been characterized by almost monotonic thickening of the active layer over the 1999–2012 period. However, after reaching its maximum in 2012, the ALT decreased for three consecutive years (Fig. 5.23). In central Siberia (Low Yenisey region) ALT increased by 0.07–0.10 m, while ALT in the East Siberian region (Yakutsk) was largely unchanged from 2014 values. In northeastern Siberia, ALT in 2015 was 4% lower than the 2014 peak values. Similarly, in Chukotka (Russian Far East) 2015 ALT values were on average 2% lower than in 2014 (Fig. 5.23).

However, ALT was still greater in 2012–15 than the long-term average value. The summer of 2014 was particularly warm in the Nordic countries and contributed to the thickest active layer measured to date at some places. On Svalbard (Janssonhaugen) ALT increased by 10% in 2015 compared to the 2000–14 mean and was the highest in the entire 1998–2015 observational record.

j. Ozone and UV radiation—G. Bernhard, I. Ialongo, J.-U. Grooß, J. Hakkarainen, B. Johnsen, G.L. Manney, V. Fioletov, A. Heikkilä, K. Lakkala

The minimum Arctic daily total ozone column (TOC) measured by satellites (Levelt et al. 2006) in March 2015 was 389 Dobson Units (DU). Measurements from March are used for assessing the temporal evolution of Arctic ozone because chemically induced loss of ozone typically peaks in the month of March (WMO 2014). The March 2015 value was 17 DU (5%) above the average of 372 DU for the period of available measurements (1979–2014) and 23 DU (6%) above the average for the past decade, 2005–14 (Fig. 5.24). The record low was 308 DU in 2011. Figure 5.24 also indicates that the Arctic ozone interannual variability is large: the standard deviation for the period 1979–2014 is 35 DU. This large variability is caused by dynamical effects that affect vortex size and longevity, transport of ozone into the lower stratosphere, and stratospheric chemistry via its sensitivity to temperature (e.g., Tegtmeier et al. 2008; WMO 2014).

Between December 2014 and April 2015, ozone concentrations measured at an altitude of 20 km by the Microwave Limb Sounder (MLS) aboard the *Aura* satellite were the highest in the MLS record, which started in August 2004 (Manney et al. 2015). The altitude of 20 km is representative of the lower stratosphere (altitude range of 15 km to 25 km) where chemical destruction of ozone is typically observed in spring when temperatures drop below –78°C (equal to about –108°F or 195 K). Chemically induced loss of ozone was minimal in the spring of 2015 because of a minor sudden stratospheric warming (SSW) event in early January. This event caused lower stratospheric temperatures to rise above the critical temperature for the formation of polar stratospheric clouds, which is a prerequisite for heterogeneous chemical reactions that destroy ozone. A second reason for the abnormally high ozone concentrations observed in 2015 was larger-than-usual transport of ozone-rich air into the lower stratosphere from higher altitudes, as observed by MLS (Manney et al. 2015). As a consequence, TOCs in the spring of 2015 were relatively high (Figs. 5.24, 5.25b).

Spatial deviations of monthly average TOCs from historical (2005–14) means were estimated with measurements by the Ozone Monitoring Instrument (OMI), which is collocated from MLS on the *Aura* satellite (Figs. 5.25a, 5.25b). Monthly average TOCs for March 2015 exceeded historical means by more than 10% over Iceland, southern Greenland, the Davis Strait between Greenland and Canada, and eastern Canada (Fig. 5.25a). In contrast, TOCs over most of Siberia were 2.5%–7.5% below the 2005–14 average

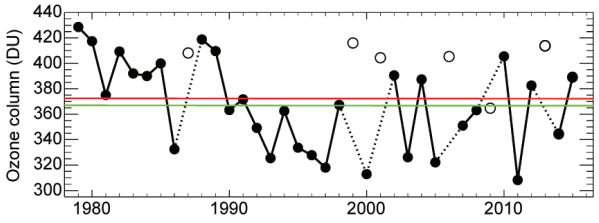

Fig. 5.24. Time series of area-averaged minimum total ozone (DU) for Mar in the Arctic, calculated as the minimum of daily average column ozone poleward of 63° equivalent latitude (Butchart and Remsberg 1986). Open circles represent years in which the polar vortex broke up before Mar. Ozone in those years was relatively high due to mixing with air from lower latitudes and higher altitudes and a lack of significant chemical ozone depletion. Red and green lines indicate the average TOC for 1979–2014 and 2005–14, respectively. [Sources: Data are adapted from Müller et al. (2008) and WMO (2014), updated using ERA-Interim reanalysis data (Dee et al. 2011). Ozone data from 1979 to 2012 are based on the combined total column ozone database version 2.8 produced by Bodeker Scientific (www.bodekerscientific.com/data/total-column-ozone). Data for 2013–15 are from OMI.]

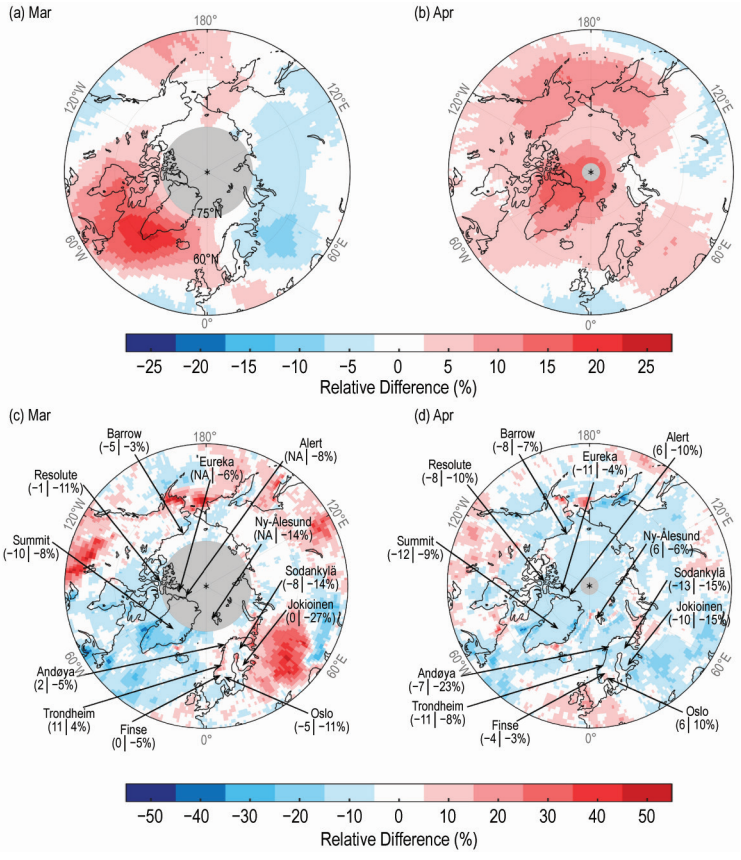

Fig. 5.25. Anomalies of total ozone column and the noontime UV index in 2015 relative to 2005–14 means. TOC anomaly for (a) Mar and (b) Apr. UVI anomaly for (c) Mar and (d) Apr (first value in parenthesis). Data are based on measurements from the OMI. Monthly means calculated from OMTO3 Level 3 total ozone products (Bhartia and Wellemeyer 2002) that are provided in 1° × 1° spatial gridding. (c) and (d) also indicate UVI anomalies measured by ground-based instruments at 12 locations (second value presented). Gray shading indicates areas where no OMI data are available.

with somewhat larger negative departures east of Moscow. Monthly average TOCs for April 2015 were above 2005–2014 means over almost the entire Arctic (Fig. 5.25b). Positive TOC anomalies between 10% and 20% were observed at the North Pole, northern Greenland, and the Canadian Arctic Archipelago.

UV radiation is quantified with the UV index (UVI), a measure of the ability of UV radiation to cause erythema (sunburn) in human skin (WHO 2002). In addition to its inverse dependence on TOC, the UVI depends greatly on the sun angle, cloud cover, and surface albedo (Weatherhead et al. 2005). In the Arctic, the UVI ranges from 0 to about 7, with sites closest to the North Pole having the smallest peak radiation and UVI values <4 all year. UVI values <5 indicate low to moderate risk of erythema (WHO 2002).

Maps shown in Figs. 5.25c,d quantify differences of monthly average noontime UVIs from historical (2005–14) means for March and April and are based on observations derived from OMI. The OMI UV algorithm uses a surface albedo climatology (Tanskanen et al. 2003) that does not change from year to year. At places where the actual surface albedo deviates greatly from the OMI albedo climatology (e.g., when snowmelt occurred earlier than usual), OMI UVI data may be biased by more than 50%, although differences in absolute values rarely exceed 2 UVI units (Bernhard et al. 2015). Figures 5.25c,d therefore also compare UVI anomalies measured by OMI and ground-based instruments deployed throughout the Arctic and Scandinavia. Anomalies derived from the two datasets agree to within ±12% at all locations, with the exception of Andøya for April (OMI overestimates the actual anomaly by 16%) and Jokioinen for March (overestimate by 27% or 0.3 UVI units). The large discrepancy for Jokioinen can be explained by early snowmelt on 9 March while the OMI climatology assumes snow cover through the month of March. Persistent cloud cover in the second half of March also contributed to this discrepancy.

Monthly average noontime UVIs for March 2015 were below the 2005–14 means in a belt stretching from the Greenland Sea and Iceland in the east to Hudson Bay and the Canadian Arctic Archipelago in the west (Fig. 5.25c). This region roughly agrees with the region where TOCs were abnormally high in March 2015 (Fig. 5.25a), but UVI anomalies show a larger spatial variability than TOCs because of their added dependence on cloud cover. Monthly average noontime UVIs for April 2015 were 5%–15% below the 2005–14 means over almost the entire Arctic (Fig. 5.25d), consistent with the positive ozone anomalies observed in this month (Fig. 5.25b).